In presenting the dissertation as a partial fulfillment of the requirements for an advanced degree from the Georgia Institute of Technology, I agree that the Library of the Institute shall make it available for inspection and circulation in accordance with its regulations governing materials of this type. I agree that permission to copy from, or to publish from, this dissertation may be granted by the professor under whose direction it was written, or, in his absence, by the Dean of the Graduate Division when such copying or publication is solely for scholarly purposes and does not involve potential financial gain. It is understood that any copying from, or publication of, this dissertation which involves potential financial gain will not be allowed without written permission.

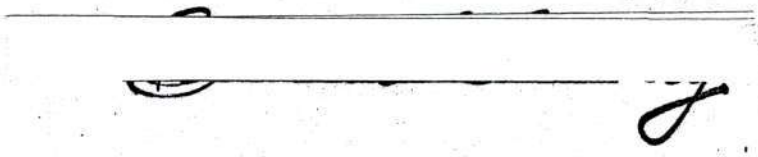

7/25/68

DIFFUSION OF KRYPTON AND NEON THROUGH ALUMINUM OXIDE

A THESIS

Presented to

the Faculty of the Graduate Division

by

Edward Lee Bradley

In Partial Fulfillment

of the Requirements for the Degree

Master of Science in Ceramic Engineering

Georgia Institute of Technology

August, 1968

DIFFUSION OF KRYPTON AND NEON THROUGH ALUMINUM OXIDE

Approved:

Date Approved by Chairman: April 1, 1969

ACKNOWLEDGMENTS

The author wishes to express his sincere appreciation to Dr. Willis E. Moody of the School of Ceramic Engineering for his guidance and patience in the course of this investigation. He is also indebted to Mr. Thomas Macrovitch, Technician of the School of Ceramic Engineering, Georgia Institute of Technology, for his skillful help and encouragement. Also, he is indebted to Mr. R. W. Buck, co-worker and companion, for his cooperation in sharing equipment and work facilities.

The financial support of the National Science Foundation and the use of the laboratory facilities of the Engineering Experiment Station and the School of Ceramic Engineering at the Georgia Institute of Technology are gratefully acknowledged.

Finally, the author wishes to express special appreciation to his wife and typist, without whose untiring effort and encouragment this work could not have been completed.

TABLE OF CONTENTS

LIST OF TABLES

LIST OF ILLUSTRATIONS

LIST OF ILLUSTRATIONS (Continued)

SUMMARY

The transport rates of neon and krypton through a specimen of polycrystalline hot pressed alumina and through a single crystal of synthetic sapphire were measured in the temperature range of 1000°C to 1200°C. A technique for mounting steady state specimens first used by Campbell[31] and later by Hurst[32] was employed together with an improved furnace design to heat the specimens and expose them to inert gases under controlled pressure gradients.

A gas flow calibration system was designed and used in conjunction with a Bendix time-of-flight mass spectrometer to measure rates of transport of the two inert gases through the alumina specimens. The diffusion equations describing the rates of transport of neon through a polycrystalline and a single crystal specimen were determined to be respectively:

$$D = 3.8 \times 10^{-7} \exp - 0.73 \text{ ev/kT} \quad \text{and}$$

$$D = 7.7 \times 10^{-6} \exp - 0.33 \text{ ev/kT}$$

The equations for transport of krypton through the same polycrystalline and single crystal specimens were determined to be respectively:

$$D = 1.9 \times 10^{-8} \exp - 1.02 \text{ ev/kT} \quad \text{and}$$

$$D = 1.2 \times 10^{-9} \exp - 0.41 \text{ ev/kT}$$

An attempt was made to verify the above results for krypton diffusion by use of X-ray fluorescence spectroscopy to measure the non-steady-state diffusion of krypton through the two alumina materials. This

technique failed to give consistent measurements of krypton in these specimens possibly due to lack of sensitivity of the detection equipment. Theoretical calculations of activation energies for diffusion of neon and krypton through a plane of HCP oxygen atoms along vacancy and edge dislocation lattice defects gave values one to two orders of magnitude higher than those measured.

CHAPTER I

INTRODUCTION

Modern technological demands have caused the utilization of many materials to surge far ahead of basic knowledge about them. One such material is aluminum oxide. Its well known properties of refractoriness, high electrical resistance, good mechanical strength, and resistance to abrasion have greatly widened its sphere of utilization during the past few years. Some of its recent applications have presented a need for knowledge of properties hitherto incompletely investigated. One such need is in the area of gaseous diffusion through alumina.

The specific purpose of this study was to determine from experimental data the diffusion constants and activation energies for neon and krypton through a hot pressed polycrystalline alumina ceramic and an alumina single crystal in the temperature range of 1000°C to 1200°C. From the magnitudes of the activation energies, the predominant mechanism of diffusion through each alumina material was postulated.

CHAPTER II

REVIEW OF THE LITERATURE

General

A recently published bibliography[1] on the subject of diffusion in ceramic systems lists 165 published contributions of 232 authors. These publications attest to the interest being shown in diffusion in ceramics. A review of the literature reveals that much work has been done on the theory of diffusion in solids in regards to the mechanisms of mass transport and their relationships to mathematical models. The ceramic materials which have been studied for better understanding of their diffusion properties are quite varied.

Mechanisms of Diffusion

Dense alumina materials are close to theoretical density and the probability is very low for ordinary flow processes such as molecular effusion, molecular streaming, streamline flow, and turbulent flow. By definition, in the diffusion process, the path diameter has been reduced to an order of magnitude near to the size of the diffusing particle. Diffusion transport is a process which is terminated by an equalization of concentrations within a single phase. The laws of diffusion connect the rate of flow of the diffusing substance with the variables responsible for this flow[2]. The means by which diffusion occurs may vary slightly between the polycrystalline and single crystalline materials because of

differences in their defect structures. Quite simply stated, the polycrystalline material is an assembly of many randomly oriented single crystals. The distinguishing differences is the tremendous number of grain boundaries possessed by the polycrystalline solid, whereas the single crystal may be thought of as one large grain which has its own internal defects, such as dislocations and vacancies. These boundaries or interfaces between grains have a marked effect upon the properties of polycrystalline materials. One of the less complex types of interfaces is the boundary between two crystals of the same material such as is found in polycrystalline alumina material. If one were to take two single crystals of exactly the same orientation and put them together they would fit perfectly; however, if the crystals are tilted slightly and then brought together, there is a disregistry at the interface which is equivalent to insertion of a row of dislocations. The number of these dislocations and the energy of the boundary increases as the angle of tilt between the crystals increases. If the two grains are rotated instead of being tilted, a grid of screw dislocations is formed. A combined tilt and rotation corresponds to a complex combination of edge and screw dislocations[3]. These screw and edge dislocations are efficient diffusion paths. Polycrystalline ceramics, which are compacts of finely divided, randomly oriented particles, thus contain a large number of these means for mass transport.

In addition to the grain boundary type of defects, there are lattice defects. When an atom moves from its normal position to an interstitial lattice position, leaving a hole in the normal position,

the resultant is called a Frenkel defect. If there is a vacant lattice site, it is called a Schottky defect. A third possible type, known as the anti-Schottky defect, would be an interstitial ion placement with no hole, or the hole could be thought of as having diffused to the surface[4]. Figure 1 shows idealized schematics of the defects.

An atom is said to diffuse by an interstitial mechanism when it passes from one interstitial site to one of its nearest-neighbor interstitial sites without permanently displacing any of the matrix atoms. Figure 2 shows schematics of diffusion mechanisms. Figure 2-A illustrates an interstitial atom in the (100) plane of a group of spheres packed into an fcc lattice. Before the atom labeled 1 can jump to the nearest-neighbor site 2, the matrix atoms labeled 3 and 4 must move apart enough to allow it through. If atom 1 rises out of the paper slightly as it starts toward atom 2, there is a partially formed channel available. Nevertheless, an appreciable local dilation of the lattice must occur before the jump can occur. If the diffusing interstitial atom is almost as large as the atoms on the normal lattice site, then the distortion of the matrix atoms involved in this mechanism becomes energetically unfavorable and another diffusion mechanism becomes dominant. In all crystals some of the lattice sites are unoccupied. These unoccupied sites are called vacancies. If one of the atoms on an adjacent site jumps into the vacancy, the atom is said to have diffused by a vacancy mechanism. Figure 2-B shows the type of constriction which hinders motion of an adjacent atom into a vacancy in a fcc lattice. If the undistorted lattice is taken to consist of close packed spheres of diameter d, the distance

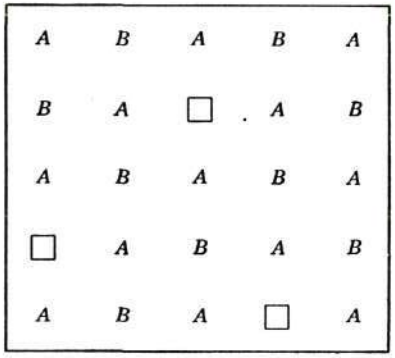

Schottky Defect

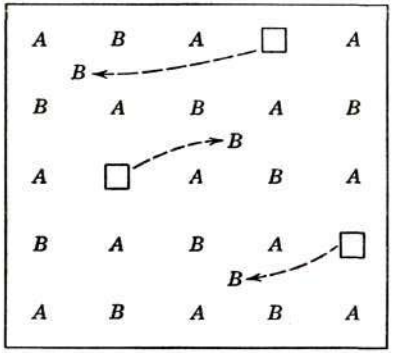

Frenkel Defect

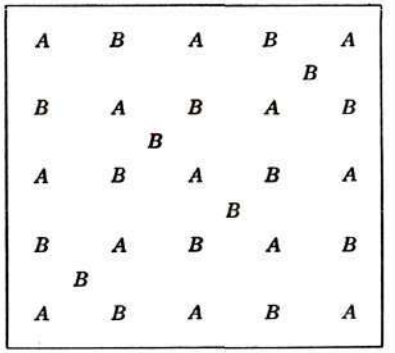

Anti-Schottky Defect

Figure 1. Lattice Defects

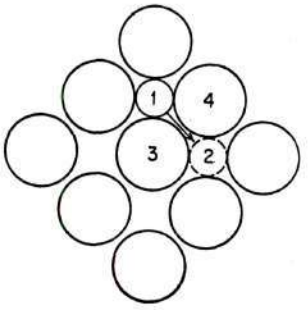

A. Movement of Interstitial Atom to a Nearest-Neighbor Interstitial Site

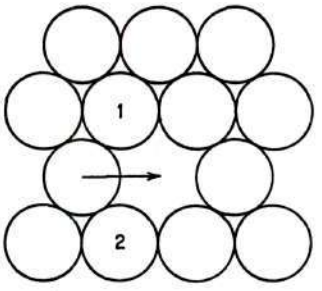

B. Movement of an Atom to an Adjacent Vacant Lattice Site

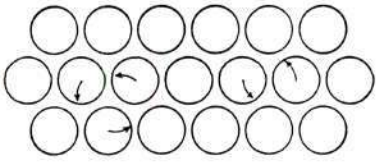

C. Self-Diffusion by Ring Rotation and Simple Exchange Mechanism

Figure 2. Diffusion Mechanisms

between the restraining atoms labeled 1 and 2 in Figure 2-B is 0.73d. The distortion required to move an atom is thus small. The vacancy mechanism has been shown to be operative in ionic compounds and oxides[5]. The ring mechanism illustrated in Figure 2-C possibly accounts for some diffusion in solids. At first, it was thought that some self-diffusion in solids occurred by a simple exchange of two nearest neighbors, but the amount of lattice distortion required for this process makes it highly unlikely. In 1950, Zener[6] pointed out that the distortion of the simple exchange could be appreciably reduced if, instead of two atoms interchanging, three or four atoms rotated as a group. He found that the activation energies for processes of this type do not appear to be vastly greater than those for vacancy diffusion in metals like copper.

The Mathematics of Diffusion

When applied to diffusion processes, Fick's first law may be stated as follows:

> The quantity of diffusing material which passes per unit time through a unit area normal to the direction of diffusion is proportional to its concentration gradient[7]. This is shown by:

$$J = - D \frac{\partial C}{\partial x} \qquad (1)$$

where J = the flux (quantity per unit time per unit area) of the diffusing substance

$\frac{\partial C}{\partial x}$ = the concentration gradient of the diffusing substance across a planor barrier

D = a proportionality factor called the diffusion coefficient

One can determine the change in concentration at any point with time during a diffusion process by determining the difference between the flux into and the flux out of a given volume element. If one considers the two parallel planes separated by a distance dx, as illustrated in Figure 3, the flux through the first plane is $J_1 = - D \frac{\partial C}{\partial x}$ and the flux, J_2, through the second plane is:

$$J_2 = J_1 + \frac{\partial J_1}{\partial x} dx = - D \frac{\partial}{\partial x} (D \frac{\partial C}{\partial x}) dx \qquad (2)$$

and by subtraction:

$$\frac{\partial J_1}{\partial x} = - \frac{\partial}{\partial x} (D \frac{\partial C}{\partial x}) \qquad (3)$$

Since the change in flux with distance equals the change in concentration as a function of time, $- \frac{\partial C}{\partial t}$, then substitution results in Fick's second law:

$$\frac{\partial C}{\partial t} = \frac{\partial}{\partial x} (D \frac{\partial C}{\partial x}) \qquad (4)$$

With D constant and independent of the concentration, this can be written:

$$\frac{\partial C}{\partial t} = D \frac{\partial^2 C}{\partial x^2} \qquad (5)$$

For steady state conditions of diffusion, that is when the flux leaving the barrier has become equal to the flux entering, $J_1 = J_2$, $\frac{\partial C}{\partial t} = 0$ and

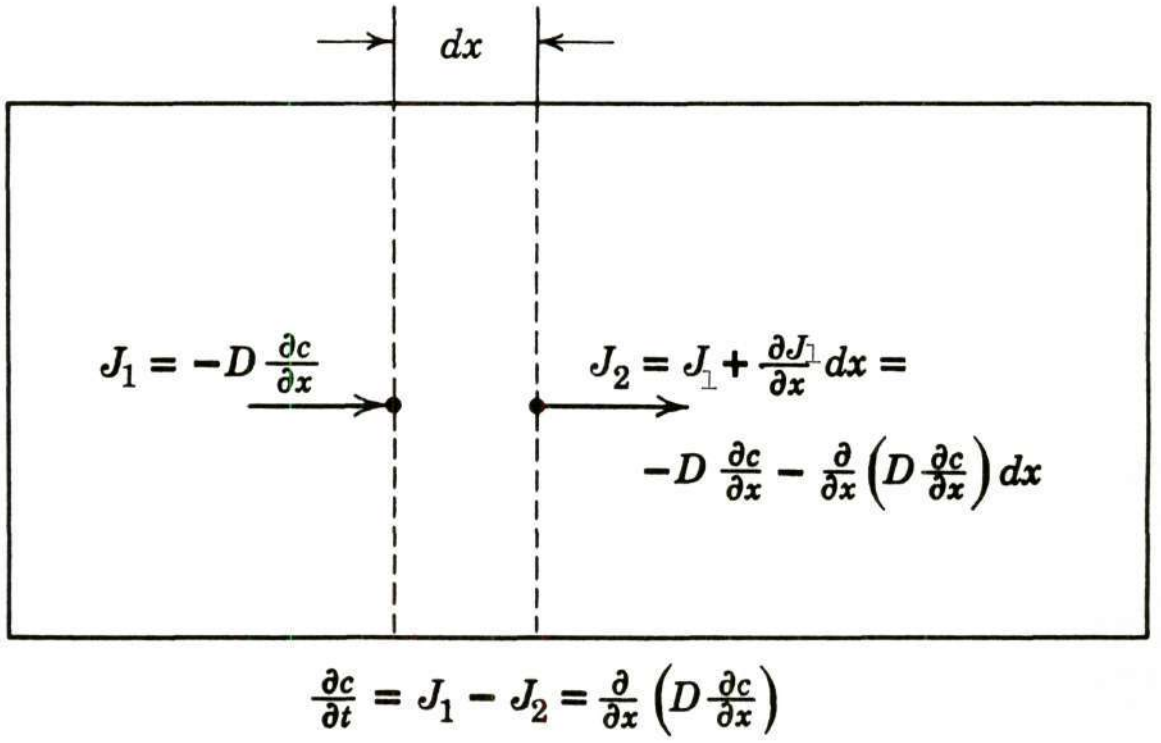

Figure 3. Diffusion Across a Planor Barrier

$D \frac{\partial C}{\partial x}$ is constant and equal to $- J_1$ and $- J_2$. It may be written that:

$$D \frac{(C_2 - C_1)}{\Delta x} = - J_1 = - J_2 \qquad (6)$$

where C_2 = the concentration of diffusing atoms on the high pressure side of the diffusion barrier

C_1 = the concentration on the low pressure side

Δx = the thickness of the barrier

Non-steady-state diffusion is characterized by the situation in which the dimension in the direction of diffusion is large compared to the distance over which measurable composition change occurs during the time of the experiment. Initially, the gas and the solid are uniform and the boundary is sharp. The surface is considered as being brought instantaneously at the beginning of the experiment to a specific surface concentration, C_s, which is held constant during the whole time of the experiment. These boundary conditions imposed upon the system may be written:

$C = C_o$ (at time t = zero and x is between zero and infinity) (7)

$C = C_s$ (at thickness x = zero and t is between zero and infinity)

$C = C_x$ (at thickness x and time t)

The mathematical problem is to solve Equation 5 corresponding to these boundary conditions. The solution given in several treatises[8, 9, 10] on the mathematics of diffusion is:

$$\frac{C_x - C_o}{C_s - C_o} = 1 - \frac{2}{\sqrt{\pi}} \int_o^{x/2\sqrt{Dt}} e^{-P^2} dP = 1 - \sigma\,(x/2\sqrt{Dt}\,) \qquad (8)$$

The concentration function $(C_x - C_o)/(C_s - C_o)$ may be visualized by remembering that each point of the specimen starts with an initial concentration C_o and after a very long time approaches a final concentration C_s. The fraction of this total concentration range which has been traversed in time t is equal to the concentration function appearing in the equation. The diffusion coefficient may be determined by first measuring the concentration C at the surface and at incremental x depths beneath the surface of the specimen. The ratio $(C_x - C_o)/(C_s - C_o)$ is then calculated for each concentration determination. Figure 4 gives the relationship of $(C_x - C_o)/(C_s - C_o)$ to $x/\sqrt{Dt}$ from Equation 8. The diffusion coefficient, D, is calculated from the Figure 4 value of $x/\sqrt{Dt}$ where x and t are experimentally measured values corresponding to the measured concentration values.

Activated Diffusion

For an atom to move from one lattice site to another in a diffusion jump, it must overcome an energy barrier, E_a, activation energy, as shown in Figure 5. Only a certain percent of the atoms in a lattice will have sufficient energy at a given temperature to overcome the barrier. As the temperature increases the number of atoms with enough energy to surmount the barrier increases in much the same manner as the rate of a chemical reaction increases. It has been found experimentally that the relations for the diffusion coefficient D follows from the Arrhenius rate equation:

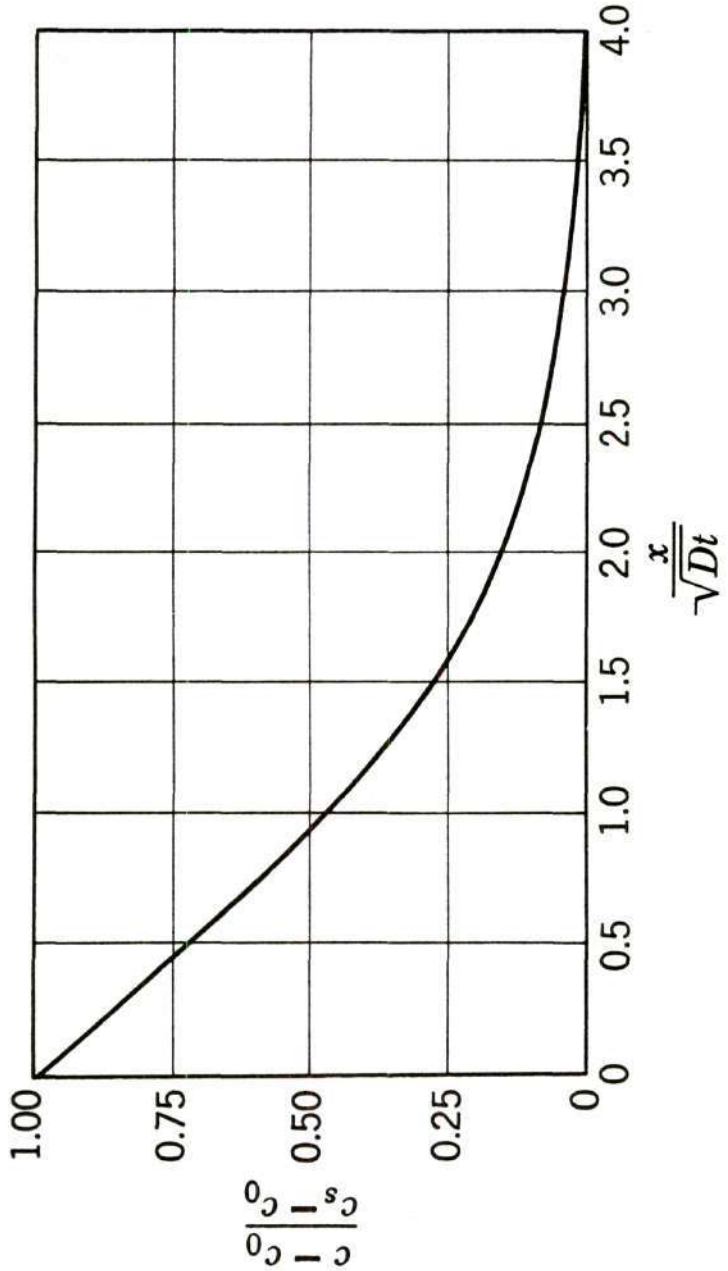

Figure 4. Penetration Curve for Non-Steady-State Diffusion

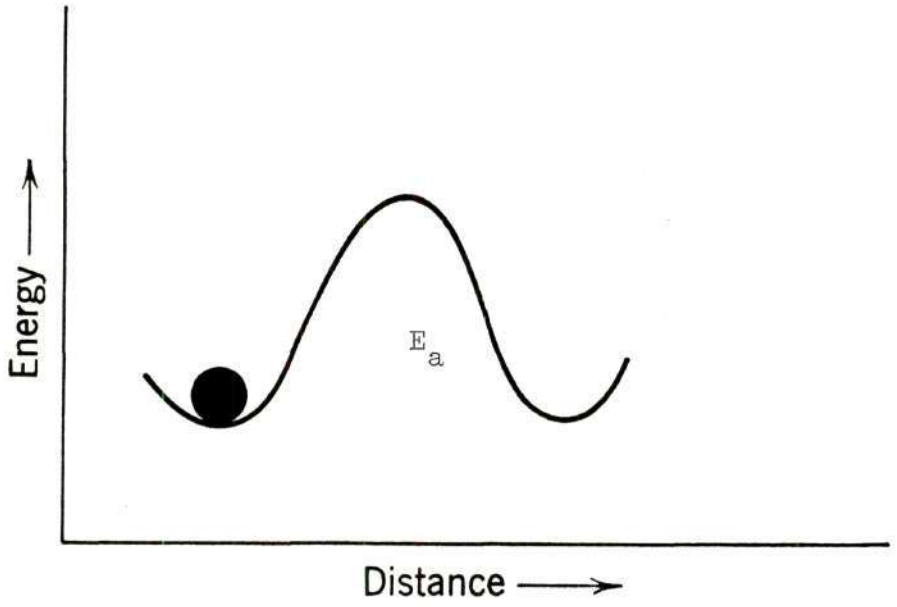

Figure 5. Diffusion Energy Barrier

$$A = A_o \exp(-Q/RT) \tag{9}$$

such that:

$$D = D_o \exp(-E_a/kT) \tag{10}$$

where E_a = the activation energy

k = Boltzmann's constant

T = absolute temperature

Taking the natural logarithm of Equation 10 gives:

$$\ln D = \ln D_o - E_a/k(1/T) \tag{11}$$

An arithmetic plot of ln D versus 1/T yields a straight line with its slope a function of the activation energy and the Boltzmann constant.

The diffusion constant D_o may be found by calculation or by extrapolating the straight line mentioned above. Values of D_o reported for a number of metals have been of the order of 10^{-2} $cm^2/sec.$, but some have deviated appreciably from this due to the approximate nature of the calculations and the assumption that E_a is independent of the temperature.

Zener[11] has shown that in inhomogeneous structures, such as polycrystalline materials and single crystals with vacancies and dislocations, the possibility exists that there are certain paths along which diffusion will have a lower activation energy than through an ordered structure of the same material. Since at any one time a fraction of the solute atoms will be in these paths of rapid diffusion, the associated D_o will be less

than that corresponding to homogeneous diffusion.

Single Crystal Alpha Alumina

The compound alpha alumina occurs in nature as the mineral corundum. A dark variety of the natural mineral containing magnetite is called emery and is used as an abrasive. Two familiar gem varieties are sapphire and ruby, both of which usually contain minute quantities of impurities which give them their colors. These natural corrundum crystals have apparently grown from melts. Large, synthetic single crystals are grown from high purity aluminum alum powder by a modified Verneuil flame process[12].

In crystals of sapphire, the oxygen ions are very nearly in hexagonal closest packing with aluminum ions located in the octahedral interstices of the oxygen framework. Figure 6 shows that the normal distribution of aluminum ions forms a simple hexagonal layer structure. It also shows that the arrangement of filled and unfilled interstices is an ordered one. In the hexagonal closest packed arrangement the third layer lies directly above the first. Accordingly, the octahedral interstices between the second and third layers are directly above those between the first and second layers; therefore, all of the hexagonal arrangements of interstices lie directly above or below one another forming the points of a simple hexagonal lattice. Figure 7 shows the distribution of cations on this simple lattice. One-third of the octahedral interstices are vacant and are called holes. The other two-thirds are occupied by aluminum ions. A hole may be considered as a region of

Al ions are small closed circles.

Holes are small open circles.

Oxygen ions are large open circles.

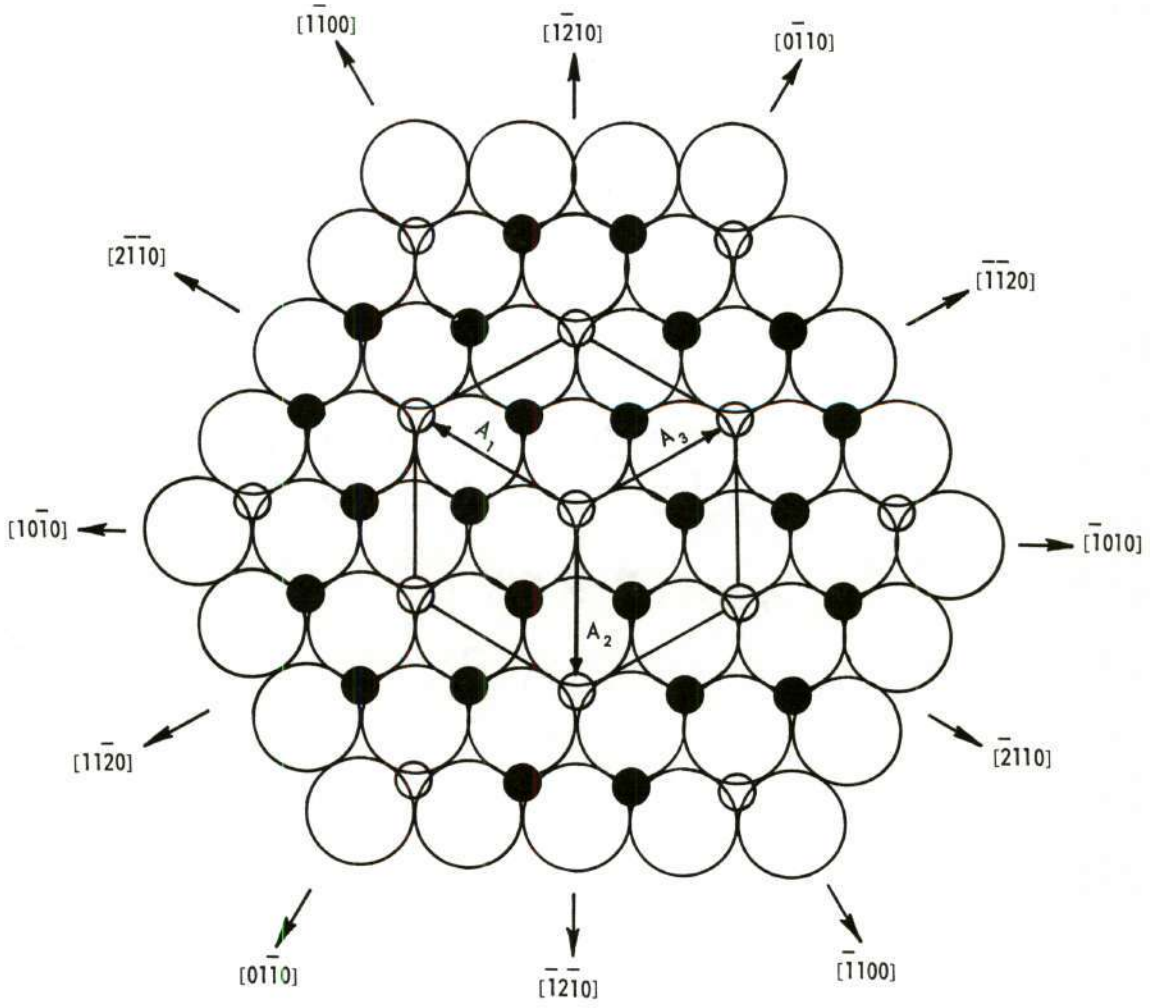

Figure 6. Basal Plane of Alpha Al_2O_3

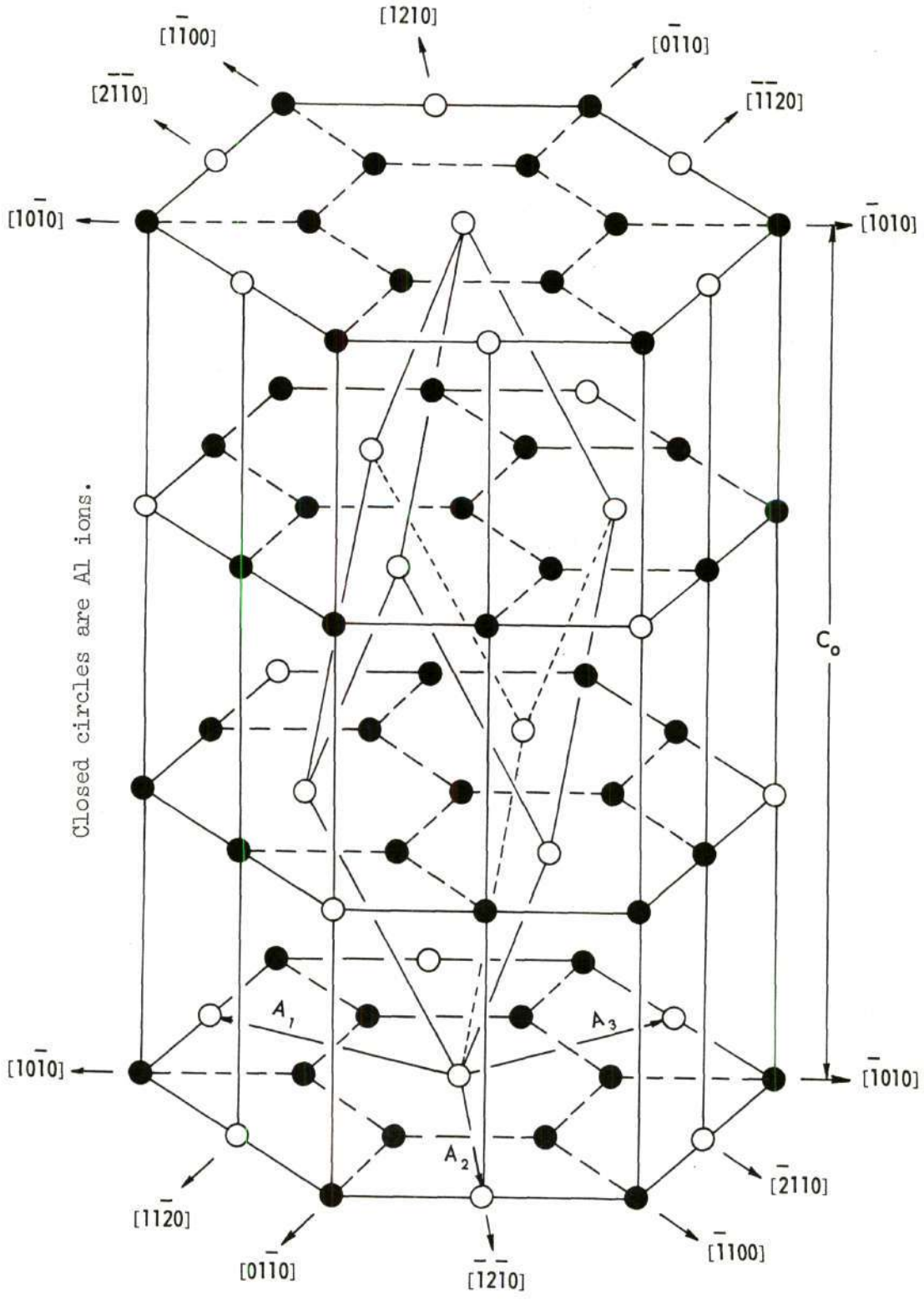

Figure 7. Lattice Distribution of Al Ions and Holes in Alpha Al_2O_3

localized negative charge, for it is surrounded solely by outer electrons of adjacent oxygen atoms. In the arrangement shown in Figure 7, the aluminum ions and holes are positioned within their hexagonal framework so as to give a maximum separation of like charges and a minimum seperation of unlike charges, consistent with the necessary bonding between oxygen and aluminum and the maintenance of gross electrical neutrality. In every layer the arrangement of aluminum ions is identical, but the layer above each preceeding layer has been translated by one oxygen-to-oxygen distance along a line parallel to the direction of closest packing in the structure. This forms a sequence in the octohedral interstices along the direction of the principle axis of two-filled-one vacant, two-filled-one-vacant, etc. There are deviations from the perfect hexagonally close packed arrangement in the real structure of corundum. For a perfect packing of spheres the packing ratio would be 1.63; whereas in corundum the ratio is 1.58. It appears that the attractive forces between the aluminum and oxygen ions are strong enough to pull the oxygen layers closer together than for perfect packing. In terms of the structural rhombohedral unit cell, the rhombohedral angle would be $53^{\circ}47'$ for perfect packing, but the observed angle is $55^{\circ}17'$[13]. Table I tabulates additional data on the corundum cyrstal structure.

Polycrystalline Hot Pressed Alumina

To describe this material, it is necessary to first mention the process of sintering. This is a process in which many small particles of some solid material are transformed into a single dense solid at some temperature below its melting point. The sintering process involves the

Table 1. Data on Corundum Crystal Structure[14]

Form	Alpha-alumina
Crystal Structure	Cr_2O_3 type
Symmetry	Hexagonal-rhombohedral
Crystal Class	Hermann-Mauguin: $\bar{3}$ m
Lattice Parameters	$a_o = 5.12$ Å, $\alpha = 55^\circ 17'$, n = 2 (rhom.)
	$A_o = 4.75$ Å, $C_o = 12.97$ Å, n = 6 (hex.)
Atomic Positions	Al: WWW; $\bar{W}\bar{W}\bar{W}$; $\frac{1}{2}$ - W, $\frac{1}{2}$ - W, $\frac{1}{2}$ - W;
	W + $\frac{1}{2}$, W + $\frac{1}{2}$, W + $\frac{1}{2}$
	O: $u\bar{u}o$; $\bar{u}ou$; $ou\bar{u}$; $\frac{1}{2}$ - u, $\frac{1}{2}$ + u, $\frac{1}{2}$;
	u + $\frac{1}{2}$, $\frac{1}{2}$, $\frac{1}{2}$ - u; $\frac{1}{2}$, $\frac{1}{2}$ - u, u + $\frac{1}{2}$
Interatomic Distances	u = 0.303 $\pm$ 0.003
	W = 0.105 $\pm$ 0.0010
Parting	Rhombohedral plane
Slip	Basal and prismatic planes
Coordination	4 Al^{3+} adjacent to each O^{2-}

initial interaction between individual particles or any material absorbed on them, followed by the construction of bonds at the points of contact. Subsequently, there is material movement into or through the region by one or more of a variety of possible mechanisms. It appears that the driving force, not considering externally applied stress, is due to the large surface energies of the small particles. The sintering process is basically a phenomenon deriving from the thermodynamic requirement for an equilibrium system that it shall achieve the maximum state of order and the minimum state of free energy. During the sintering process, there is both a general overall increase in order and a great reduction in surface free energy arising from a reduction in total surface area. Among the basic mechanisms which contribute to sintering are the following[15, 16, 17, 18, 19]:

(a) Interaction of chemical bonds between adjacent particles.

(b) Modification of these indefinite bonds to be normal lattice linkages in the zone of contact.

(c) Surface diffusion of atoms or ions into the vicinity of the zone of contact.

(d) Transfer of material into or through the zone of contact by lattice or volume diffusion.

(e) Macroscopic flow, particularly under the influence of applied mechanical stress.

(f) Recrystallization, complex nucleation, and crystal growth.

(g) Evaporation and condensation mechanism.

Of considerable practical significance in the sintering process are these factors:

(h) The effect of particle size, shape, orientation and size distribution.

(i) Pore closure of open or continuous pores.

(j) Pore closure of closed and isolated pores.

(k) Nature and type of previous or continuous mechanical stresses.

(l) Atmosphere in which the article is sintered.

(m) Type and quantity of impurities.

The hot pressing of high purity, fine particle sized, alpha-alumina incorporates most of the mechanisms listed above to some degree. Simply stated, the hot pressing operation is a method of applying simultaneously the forming pressure and sintering heat which in conventional ceramic forming operations is accomplished in two separate stages. The chief advantage of hot pressing is that near-theoritically-dense compacts may be formed without as much grain growth as is associated with ordinary firing techniques. This lack of grain growth enhances many of the mechanical and electrical properties of ceramics. The disadvantages of the hot pressing process are its slowness and the expense of the operation. Typically, the forming die is made of a material of good high-temperature strength such as graphite. The die, usually consisting of a simple thick-walled cylinder of graphite with an upper and lower plunger of the same material, is filled with the powdered material to be pressed and set inside a fused silica tube. The tube is filled with a high-temperature insulating powder such as zirconia. This assembly is placed inside an induction coil positioned beneath the plunger of a hydraulic press. While the die is heated inductively, the pressure of the press is increased to just under the high-temperature breaking point of the die. This process

takes advantage of the mechanism of macroscopic flow under the influence of applied mechanical stress which is virtually absent in the ordinary sintering process.

If a pure homogeneous polycrystalline material were divested of all of its grain boundaries, it would become a single crystal. These grain boundaries, therefore, are the key to the differences in nature of the two forms. Grain boundaries are the regions between two contiguous phases that may or may not be the same. They may be thought of as internal surfaces, since they have surface energy that appears in the form of surface tension. Grain boundaries may be formed in many different ways, including recrystallization of a solid or by sintering; but in all cases they are regions of misfit between adjacent crystalline phases. The effects of grain boundaries are varied. They greatly modify the mechanical properties of a solid. As compared to the properties of a single crystal, it will usually be found that yield and tensile strengths are greatly increased. The plasticity, as measured by the ductility and reduction in area, is markedly decreased. The cleavage or fracture strength is increased along with the fatigue strength and creep strength. All of these effects are grain-size dependent. Generally, properties that are a function of electronic energies such as electrical and thermal properties are, when compared to mechanical effects, less affected by grain boundaries. They do, however, show easily measurable differences. Since the grain boundary is a region of misfit, it must be in a condition of strain. This is confirmed by studies which indicate that the hardness of the material in a boundary is different than that in the crystal grain. Also, melting

studies indicate that grain boundaries melt before the matrix material and when acids or alkalies are applied to a polished polycrystalline surface, the grain boundaries are invariably attacked more rapidly than the crystals. Diffusion studies show that atoms move through grain boundaries at a much greater rate than through the crystal lattice[23].

Neon and Krypton

Neon and krypton are elemental, monoatomic gasses located in column VIII of the periodic table, along with helium, argon, zenon and radon. These elements form a family of so-called noble gases, each of which have a completed outer shell of eight electrons. They are called noble because of their reluctance to enter into reaction with other elements. Indeed, until recently[24], no compounds containing any of the column VIII elements were known to exist. All of them have stable isotopes except radon, which is born in the radioactive decay of radium. The properties and extents of atmospheric occurance of all of the stable noble gases are shown in Table 2 for comparison. All totaled, they constitute less than one percent of the atmosphere. Except for helium, these gases are obtained commercially by low-temperature separation of air. The primary advantage in using these noble gases in diffusion studies lies in their chemical inertness and the ability to study the diffusion properties of the alumina structures with two different sizes of atomic particles with minimum destructive alteration of the original alumina structures. In addition, there is no fire hazard in handling these gases. On the negative side is the fact that the heavier noble gases are quite expensive.

Table 2. Properties of Stable Noble Gases[25, 26]

Gas	He	Ne	Ar	Kr	Xe
Atomic No.	2	10	18	36	54
Atomic Weight	4.003	20.183	39.944	83.7	131.3
Atomic Diameter kX	1.86	3.20	3.82	4.0	4.4
Density g./l*	0.1785	0.9003	1.7839	3.745	5.897
Ionization Potential e.v.	24.580	21.559	15.755	13.996	12.127
Stable Isotopes by Mass Number and Percent Abundance	3-Tr	20-90.5	36-0.35	78-0.34	124-0.094
	4-100-	21-0.28	38-0.08	80-2.23	126-0.088
		22-9.21	40-99.6	82-11.5	128-1.92
				83-11.5	129-26.24
				84-57.0	130-4.05
				86-17.4	131-21.2
					132-26.93
					134-10.52
					136-8.93
Atmospheric Occurrence 1 Part in	200,000	65,000	106	900,000	12,000,000
Total Impurities in Gas Used p.p.m.		<10		<36	

* $0^{\circ}C$ - 760 mm Hg

Previous Studies of Diffusion in Alumina

Oishi and Kingery[27] carried out experiments with the objective of determining the effect of temperature on the diffusion coefficient of oxygen in both single-crystal and polycrystalline aluminum oxide. The stable isotope O_{18} was diffused into the alumina samples in the temperature range 1360°C to 1780°C and the diffusion rates were determined by mass spectrometric analysis of the samples. Diffusion coefficients were found to be in the range 10^{-16} to 10^{-13}. The experimental activation energy for one set of samples at temperatures below 1650°C was determined to be 57.6 kcal/mole. The variable results obtained at temperatures below 1650°C were thought to be due to impurity controlled or structure-sensitive diffusion. From their experimental results, they calculated that the energy required to form intrinsic imperfections in the aluminum oxide lattice was about 157 kcal/mole of oxygen ion vacancies and associated aluminum ion vacancies. The oxygen diffusion coefficient determined for polycrystalline alumina was nearly two orders of magnitude larger than that observed for single-crystal samples. The activation energy observed for polycrystalline alumina at temperatures above 1450°C was 110 kcal/mole. At lower temperatures variable results were obtained, presumably corresponding to impurity-controlled or structure sensitive diffusion.

Hayes, et al[28], studied the permeability of dense sintered alumina materials with oxygen, nitrogen and argon at temperatures up to 1750°C. The material being studied was formed into a closed-on-one-end, thin-walled tube which was evacuated from its open end. The specimen tube was centered axially inside a tube of sintered alumina of larger

diameter. One end of the larger tube was sealed vacuum tight to the outside of the specimen tube near its open end. The open end of the larger tube was connected to a vacuum system and gas cylinders. A molybdenum-element furnace was positioned around the central portion of the tubes. With both tubes evacuated and the furnace at the desired temperature, the gas was admitted inside the outer tube. The rate of rise in pressure within the inner specimen tube was measured with a Pirani gauge while the open end of the system was isolated from the vacuum system with a stopcock. The diffusion coefficients were evaluated from the times to reach a steady rate of permeation after admission of the gas to the outer tube, using the method of Barrer[29]. The diffusion coefficients for oxygen ranged for different specimens from 2×10^{-5} $cm^2/sec.$ to 3×10^{-6} $cm^2/sec.$ Relatively little permeation of the tubes was detected for nitrogen and none for argon. The authors suggested that some chemically sensitive diffusion process is responsible for this selective behaviour on the part of alumina toward the three gases used in these experiments.

Campbell[30] determined that a helium-leak-detector type of mass spectrometer could be used to measure the rate of diffusion of helium through thin barriers of single crystal and polycrystalline alumina. His measurements in the temperature range $200^{\circ}C$ to $700^{\circ}C$ were made by use of a specially designed specimen barrier sealed with a high-temperature bond between two thick walled alumina tubes. This barrier design will be described more fully in the section of this work titled "Preparation of Steady-State Diffusion Cells". The equation for the coefficient of diffusion of helium through single crystal alumina in the

temperature range 200°C to 700°C was found by Campbell to be:

$$D = 6.2 \times 10^{-6} \exp - 0.32 \text{ electron volts/kT} \qquad (12)$$

Campbell also found that the magnitude of the coefficient of diffusion of helium through polycrystalline alumina varies as a function of density and decreases with repeated heating. He calculated an activation energy of 0.13 electron volts for the initial heating to 500°C and 0.15 electron volts for the second cycle and attributed the change to annihilation of some grain boundary defects during the initial heating.

Hurst[31] studied helium diffusion in two different polycrystalline alumina materials, a hot-pressed alumina fabricated from particles with an average size of around .30 microns and a specially processed and sintered alumina called Lucalox made from particles of approximately 30 microns average diameter. He used the same type of diffusion cell as Campbell. Helium diffusion through the Lucalox was found to be below the sensitivity of the helium mass spectrometer in the temperature range 25°C to 900°C, indicating diffusion coefficients below 10^{-11} cm^2/sec. The hot-pressed samples yielded values of the diffusion coefficient ranging from 10^{-11} cm^2/sec. to 10^{-6} cm^2/sec. and activation energies in the range 0.222 electron volts to 0.830 electron volts.

Bendix Time-of-Flight Mass Spectrometry[32]

The Bendix time-of-flight mass spectrometer is one of the most recent designs to evolve out of the approximately 65 years of development in the field of mass spectrometry. This instrument was developed

in 1955 under the sponsorship of the Bendix Aviation Corporation and is of a non-magnetic time-of-flight type. It was made commercially available in 1957.

Basically, time-of-flight (TOF) spectrometers consist of an ion source and a collector situated at opposite ends of an evacuated "flight" tube. The ions are formed in the ionization region of the source usually by electron bombardment. They are then accelerated out of the source toward the collector by one or more electric fields. In some cases, the fields are applied continuously. In others, the accelerating fields are pulsed at the end of the ion formation portion of the cycle. If the accelerating pulse lasts until all ions have left the source, all ions receive essentially the same energy. If, with a single constant accelerating field, the ionization pulse cuts off before any of the ions leave the source, all ions receive essentially the same momentum. In either case, the velocity of the ions in the free flight path is a function of the ratio of their mass m, to their electron charge e; therefore, when the ions reach the collector they have separated into bunches corresponding to m/e. If only singly charged ions are present, the lightest group reaches the detector first and is followed by groups of successively heavier mass. Thus, each source pulse results in a mass spectrum which can easily be displayed by connecting the ion collector to the vertical plates or an oscilloscope[33].

Figure 8-A shows a schematic of the Bendix TOF mass spectrometer. This mass spectrometer operates at a repetition frequency of 10,000 cycles per second, and therefore produces 10,000 complete mass spectra each second. The first event in each cycle is the creation of the

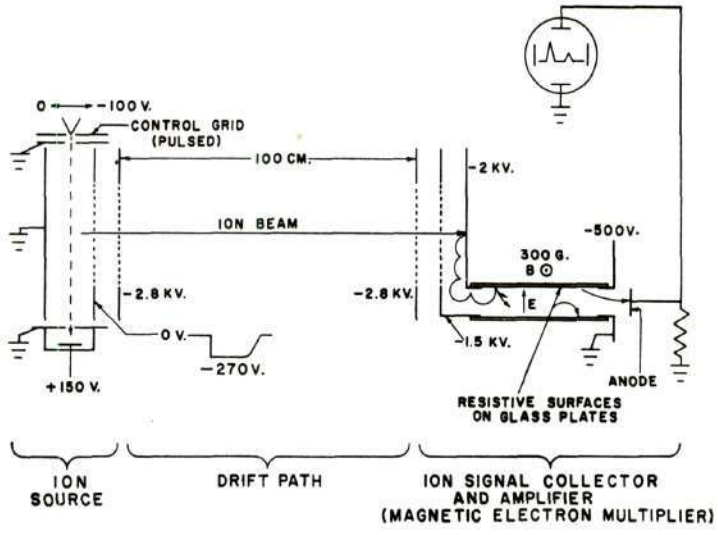

A. Schematic of Bendix Time-of-Flight Mass Spectrometer

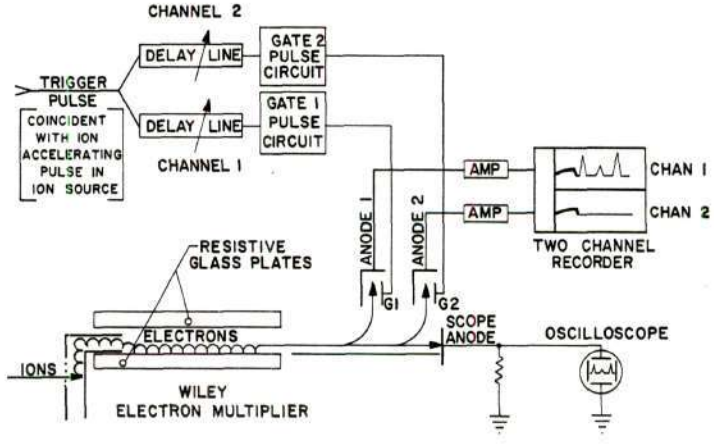

B. Schematic of Collector-Multiplier

Figure 8. Bendix Time-of-Flight Mass Spectrometer

electron beam from an internally heated tungsten wire. The electrons are normally kept from entering the ionization region by a negative bias on the control grid. At the beginning of each cycle, a 0.25 micro-second positive pulse is applied to the control grid, allowing the magnetically collimated electron beam to pass through the ionization region. The energy of the electron beam, which is variable between 0 and 100 volts, is determined by the difference between the D.C. potential on the filament and the ground potential on the second grid of the electron gun. During ionization, all elements surrounding the ionization chamber are at ground potential. Immediately after the electron beam is turned off, the first grid in the ion gun is pulsed to about -270 volts for sufficient time for all positive ions of interest to move through this grid into the accelerating region of the source. Here they are accelerated by a 2800 volt potential on the ion energy grid. This final grid in the ion gun is of the proper distance from the electron beam, and the flight tube of proper length such as to determine the time of flight. This is called the positive pulsed mode of operation. There are three other modes of operation which will not be described -- negative pulsed ions, continuous negative ions, and continuous positive ions. For the Bendix machines, the distances are arranged so as to give a time of flight in microseconds that is roughly equal to the square root of 2m/e. Mass separation results only from the mass dependent velocities; no electric or magnetic fields are used to enhance separation.

The resolving power of the instrument depends greatly upon the ability of the source to deliver the ions of each mass-to-charge ratio

to the detector (electron multiplier) in the collector end of the mass spectrometer in a tight bunch, even though they vary in initial position and velocity. Adjustment of the fields in the ionizing and accelerating regions, made by varying the height of the ion-ejecting pulse, causes a "crossover point" for the ion bunches to occur as they pass into the ion detector. This greatly improves the ability of the instrument to pick out one mass from another closely adjacent. The period of the instrument is about 100 microseconds and the time of flight of mass 5000 for an instrument with a 100 cm flight tube is about 100 microseconds; therefore, the maximum mass which can be resolved in a single cycle is 5000 a.m.u. (atomic mass units). If the flight tube is lengthened to improve resolution, the time of flight will be longer and the maximum resolvable a.m.u. proportionally smaller.

The absolute sensitivity of the instrument is such that one detected argon ion at each output cycle, or 10,000 ions each second, is produced for an argon partial pressure in the source of about 7×10^{-10} mm Hg. The relative sensitivity is such that five parts per million of tin has been seen in a sample evaporated in a vacuum furnace.

The mass spectrum produced by the electron multiplier is displayed on an oscilloscope synchronized with and triggered by the mass spectrometer. Any portion of the mass spectrum can be viewed in any desired detail by adjusting the horizontal sweep speed controls on the oscilloscope and the continuously variable delay on the spectrometer between the ion accelerating pulse and the oscilloscope trigger.

The design of the electron multiplier allows an oscilloscope display of the mass spectrum and simultaneous recording of individual

peaks or scanning of any portion or all of the spectrum. The number of individual peaks whose intensity may be recorded at one time depends upon the number of gates in the recording output section of the collector. The system shown in Figure 8-B has two gates. The electron beam within the multiplier ordinarily collects on the oscilloscope anode but, when a gating pulse is applied to either G1 or G2, the beam is collected on the corresponding anode for the duration of the gating pulse. This is ordinarily no longer each cycle than the duration of one mass signal (about 0.05 microsecond). Mass peaks are selected by choosing appropriate values of delay on each channel and the peaks of higher or lower mass may be scanned and recorded at a constant rate from a selected point if desired.

The recording is usually done on photosensitive paper by a spot of light reflected from a tiny mirror attached to a very sensitive galvanometer. Each galvanometer receives its deflecting current from its respective gate in the recording output section of the collector. The paper in the recorder may be run at any one of several constant speed settings while scanning a peak at any one of several constant scan rates. One is thus able to attach quantitative meaning to the area under the peaks traced out by the recorder.

A number of different means are available whereby samples are introduced into the mass spectrometer. Generally speaking, they are all either a means of admitting a gaseous sample from outside the instrument or else a device for forming a gas from a liquid or solid sample within the ionization region of the electron gun.

The Bendix mass spectrometer has a self-contained vacuum system consisting of a mechanical fore pump and a mercury diffusion pump equipped

with freon-refrigerated baffle and liquid-nitrogen cold trap.

X-Ray Fluorescence Spectrometry

Matter absorbs X-rays in two distinct ways, by scattering and by true absorption. The scattering of X-rays by atoms is similar in some ways to the scattering of visible light by dust particles in the air. True absorption is caused by electronic transitions within the atoms and accounts for the greater part of the total absorption. Just as an electron of sufficient energy can knock a K electron, for example, out of an atom and thus cause the emission of K characteristic radiation, so also can an incident quantum of X-rays. In the latter case, the ejected electron is called a photoelectron and the characteristic radiation is called fluorescent radiation. The emitted radiation is referred to as characteristic because each element emits a set of wavelengths of radiation which are characteristic of only that one element.

From these interactions of X-rays with elements comes the basis for a method of chemical analysis. The sample to be analyzed is placed in the fluorescent X-ray spectrometer outside the window of its X-ray tube and bombarded with X-rays as shown in Figure 9. The primary radiation causes the sample to emit its characteristic secondary radiation. The analysis is carried out by diffracting this secondary radiation from lattice planes of known d spacing in the analyzing crystal of the spectrometer. In accordance with the Bragg law, radiation of only a single wavelength is reflected for each angular setting of the crystal and the intensity of this radiation is measured with a suitable counter. The counter may be set to scan the entire spectrum or to monitor a single peak. The

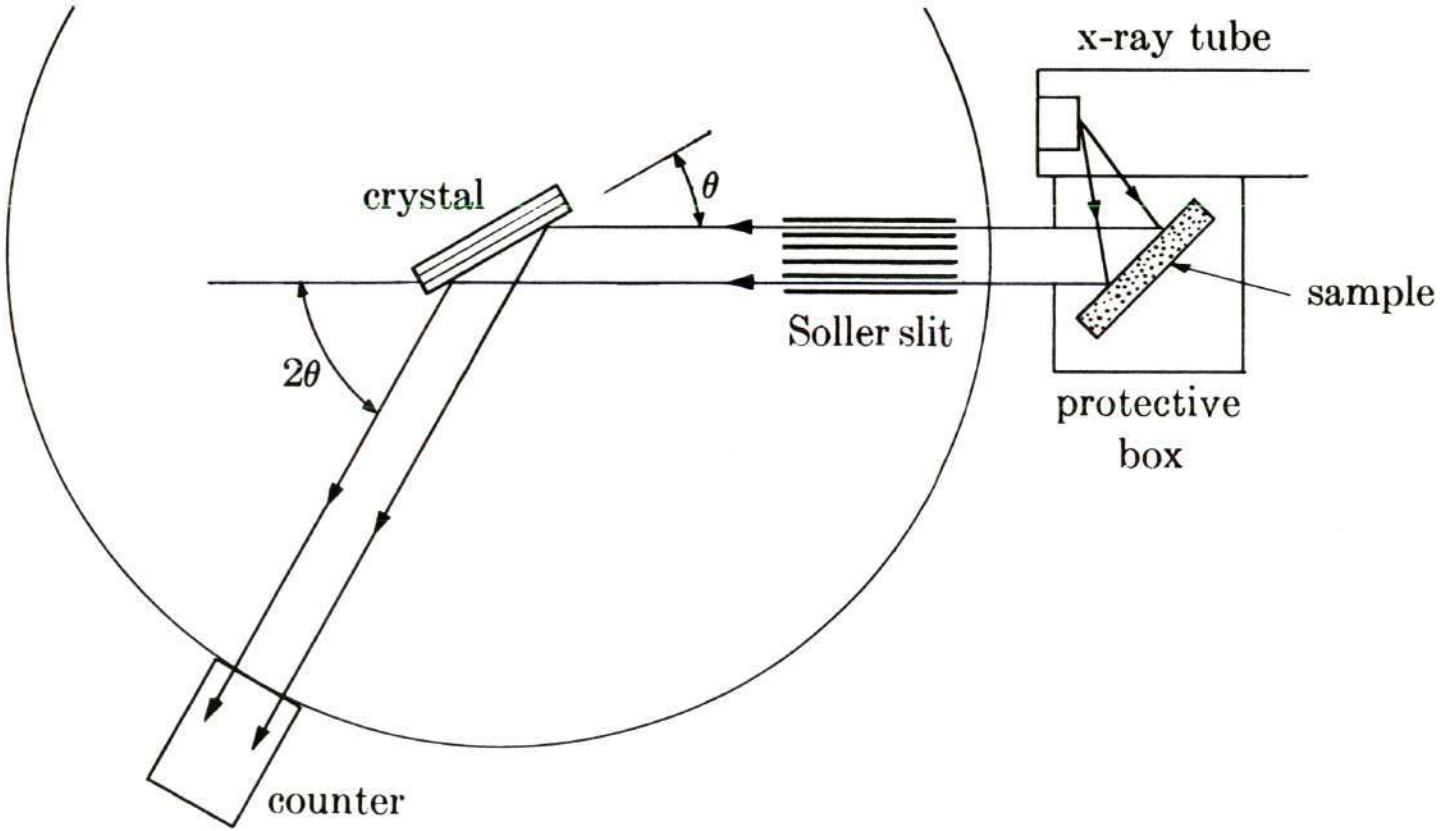

Figure 9. Schematic of X-Ray Spectrometer

analysis of the sample may be either qualitative or quantitative.

CHAPTER III

MATERIALS AND EQUIPMENT

Sources and Properties of Materials Studied

The alumina materials were purchased from two commercial sources in their most economically available forms. Inert gases were likewise obtained from a reliable commercial source. The sources and properties of each material are detailed separately.

Polycrystalline Alumina

Cylinders of polycrystalline alumina approximately four inches long by one inch in diameter were obtained from the Carborundum Company, New Products Branch, Niagara Falls, New York. They were hot-pressed by Carborundum Company from Type A-5175 alpha alumina powder from the Linde Company, 30 East 42nd Street, New York 17, New York. This powder is at least 99.9 percent purity and has an average particle size of approximately 0.3 microns[34].

Single-Crystal Alumina

Boules of synthetic sapphire in the shape of tapered cylinders, approximately two and one-half inches long and slightly over one inch in diameter at the large end, were obtained from the Linde Company. The properties of this material are listed in Table 3. The position of the C-axis was located and marked on the boules by the manufacturer to allow proper orientation for cutting.

Table 3. Properties of Linde Synthetic Sapphire[20, 21, 22]

Composition	99.988% aluminum oxide (Al_2O_3)
Crystal Structure	Hexagonal
Finish	Optically clear or frosted
Melting Point	2040°C
Hardness	Knoop: 1525 to 2000
	Mohs : 9
Specific Gravity	3.98
Specific Heat	0.18 calories per gram at 20°C
Thermal Conductivity	0.065 calories/cm^2/sec./°C/cm at 100°C
Compressive Strength	300,000 psi at 77°F
Young's Modulus	50 to 55 X 10^6 psi (dependent on position of C-Axis)
Modulus of Rupture	At 30°C, 40,000 to 130,000 psi
Sealing Characteristics	High and low temperature seals can be made to metals, glass and ceramics.

Inert Gases

High purity neon and krypton gas was purchased from the Linde Company. Table 2 lists the properties of these two gases, as well as those of the other stable inert gases for comparison.

Machining of Specimens

For steady-state polycrystalline specimens, the cylinders were cut transversely to their length into discs 5/8-inch long. Holes 1/4-inch in diameter were drilled into the center of both flat sides of the discs with a diamond core drill. The depth of these blind holes was such as to leave approximately 0.200 inch of barrier material between the bottoms of the two holes. The final thickness of the barriers was obtained with a Raytheon Model 2-334 Ultrasonic Impact Grinder, using 1/4-inch drill rod as the grinding surface and 100 mesh B_4C abrasive supplied by the Norton Company. The thickness of each barrier was checked periodically with a specially adapted micrometer as the ultrasonic grinding proceeded. A bevel of 30 degrees to the axis of the cylinder was machined on each side of the discs by means of a 100 grit diamond lap. The lap wheel was mounted on the spindle of a diamond saw manufactured by Felker, Inc., Torrance, California. The drilled discs were mounted one side at a time to 1/4-inch diameter aluminum dop sticks with sealing wax and rotated against the water-cooled diamond lap by means of a specially adapted hand drill bolted to the universal stage of the Felker machine, as shown in Figure 10. Figure 11 shows a finished polycrystalline barrier along with its refractory support tubes in assembled and disassembled positions.

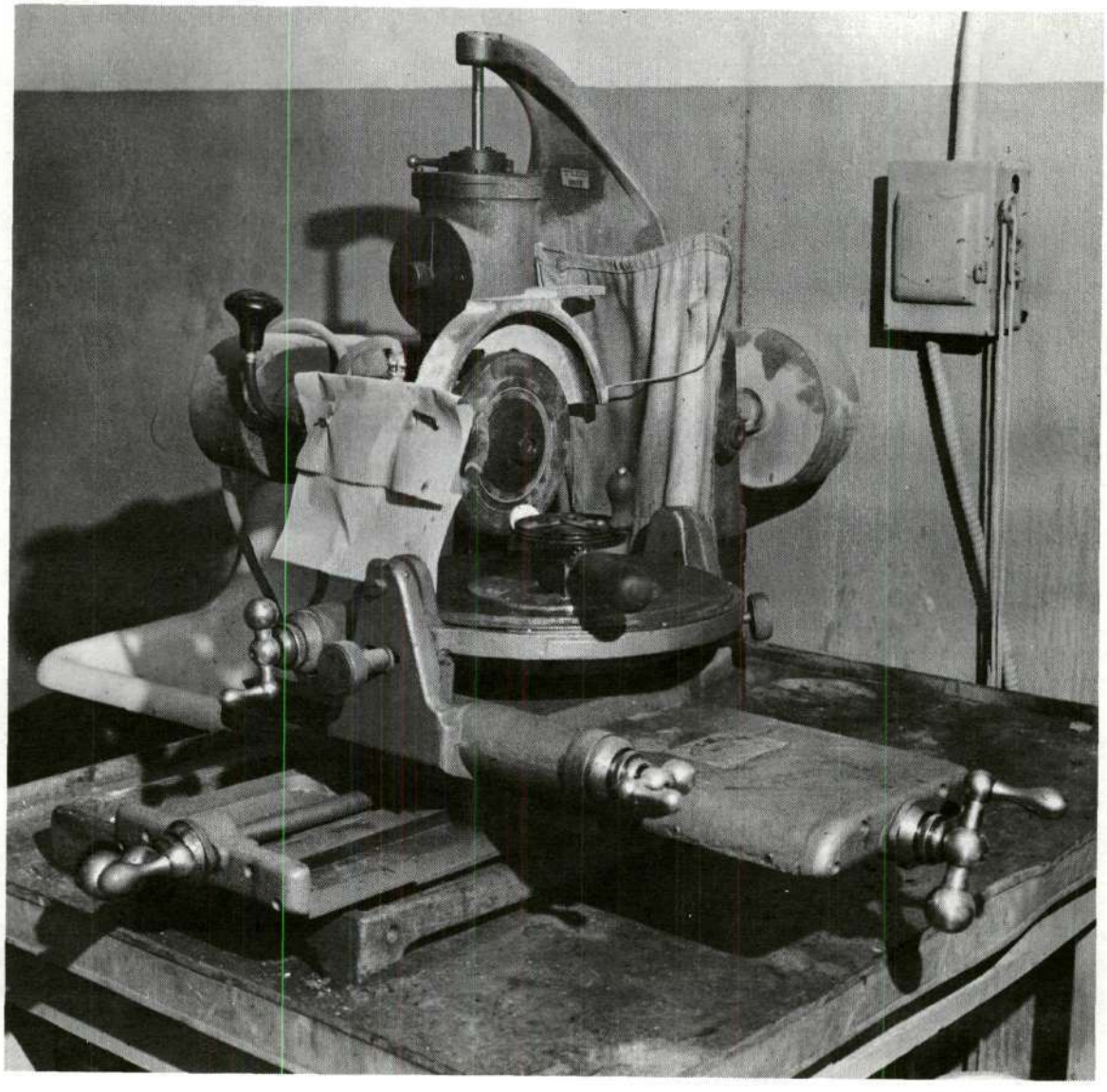

Figure 10. Diamond Lap Wheel

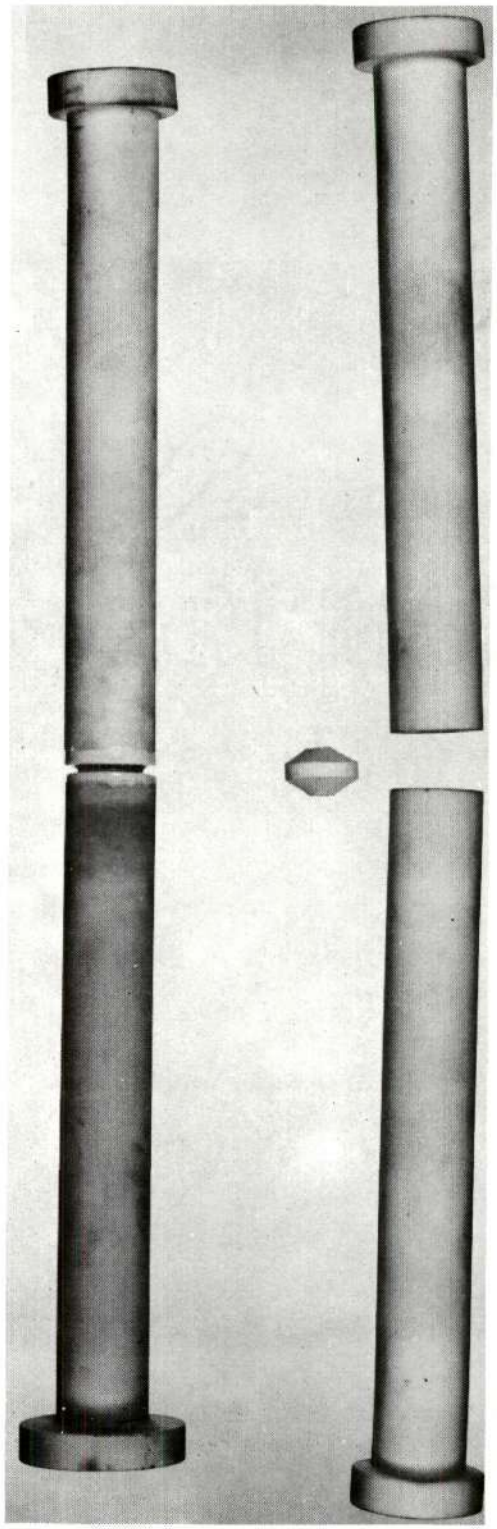

Figure 11. Diffusion Cell - Disassembled and Assembled

Single crystal steady-state barriers were machined in a like manner to the polycrystalline, with one exception. The boules were sliced perpendicular to the marked C-axis instead of perpendicular to the length of the rods as with the polycrystalline specimens. The holes drilled into the single-crystal specimens were in the same direction as the C-axis. Figure 12 shows a single-crystal barrier with a small polished window through which the bottoms of the holes in the barrier are visable.

For non-steady-state diffusion studies, rectangular blocks with dimensions of approximately 1/2" X 1/2" X 1/4" were cut from each type of alumina with a diamond saw. The surfaces of the blocks were smoothed on a 100 grit diamond lap. Orientation of the cuts on each single-crystal block was such that the C-axis was perpendicular to one of the 1/4" X 1/2" faces of the blocks.

Preparation of Steady-State Diffusion Cells

The steady-state diffusion cell shown in Figure 11 consisted of two flanged refractory support tubes between which the alumina barrier was sealed. The support tubes were of a high alumina composition, Alsimag 614, obtained from American Lava Corporation. The tubes were 9 1/2 inches long by 1 1/4 inches outside diameter, with a 1/4 inch diameter hole through the length. The flange was 1 3/4 inch diameter by 1/2 inch thick. A 30° countersink in the end opposite the flange was designed to mate with the bevel cut on the barrier. To insure a good fit between the barrier and support tubes, the mating surfaces were lapped together using 100 mesh boron carbide abrasive. After lapping, each barrier and its two support tubes were given a thorough cleaning.

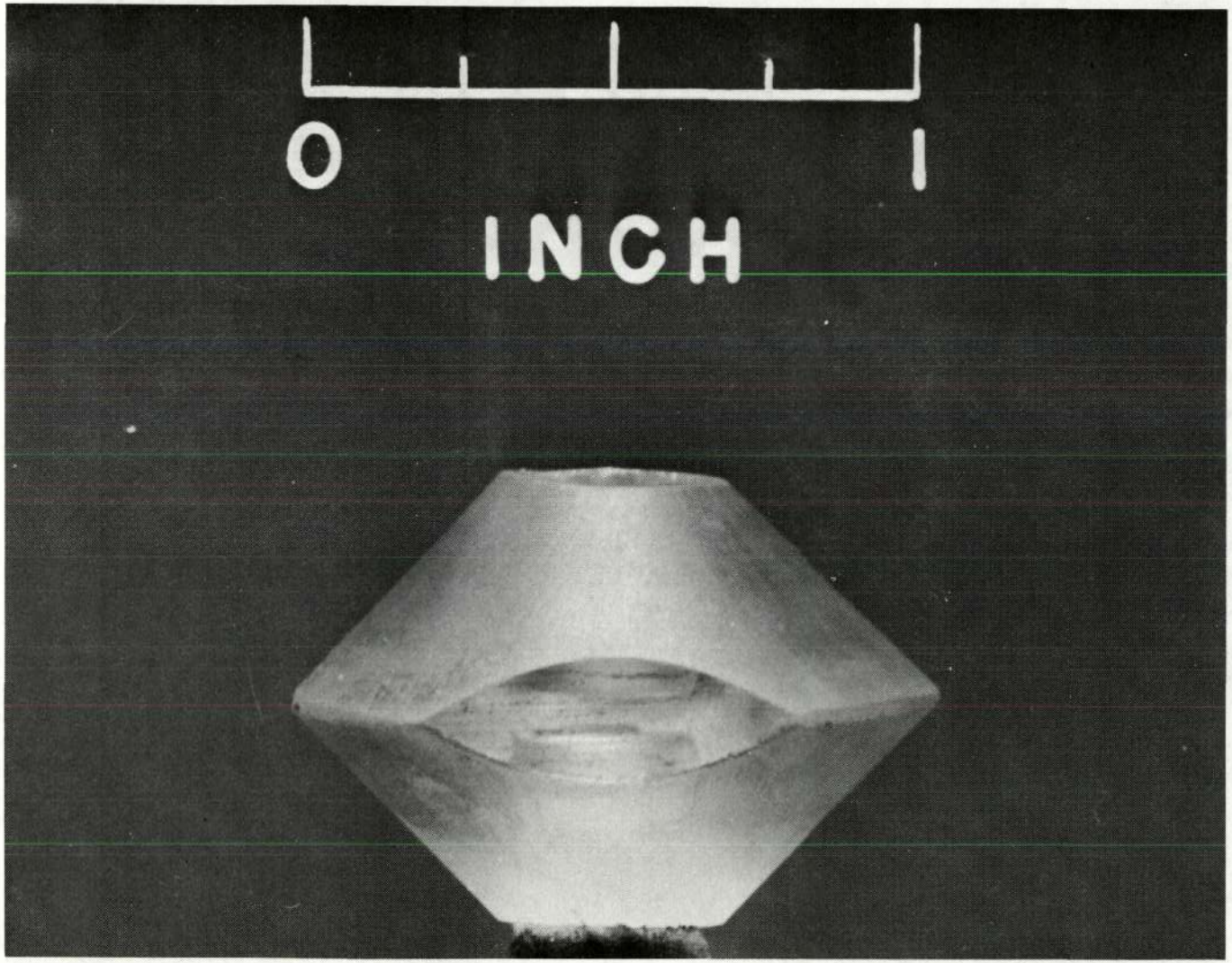

Figure 12. Single Crystal Barrier

The holes in the beveled ends of the tubes and in both sides of the barrier were stuffed with wet paper to mask them from being coated with the sealing composition applied to the beveled surfaces. The sealing composition was a high-temperature glaze-type material of composition shown in Table 4. This finely divided material was slurried with water and sprayed onto the sealing surfaces with an aspirator-type hand-spray gun. The sprayed surfaces were dried thoroughly before assembly for firing.

The cell components were assembled in a vertical position in a modified oxy-acetylene pyrometric-cone-equivalent furnace. Usually, two diffusion cells were placed into the furnace for each firing. The temperature was increased at a rate of 482°C per hour to 1482°C and allowed to cool to near room temperature before the diffusion cells were removed.

Each of the two sealing surfaces and the barrier membrane was checked independently for leaks with a Veeco Model MS-9 helium leak detector manufactured by Vacuum-Electronics Corporation, Long Island, New York.

Furnaces

Separate vacuum furnaces were designed and constructed in a local shop for the steady-state and the non-steady-state diffusion studies. Both were constructed of 3/16" rolled brass plate silver soldered at all permanent joints. They were cooled by water flowing through 1/4" outside diameter copper coils, soft soldered to the outside surfaces. Details of each furnace are presented separately below:

Table 4. High Temperature Seal Composition

Calculated Formula in Moles

RO		R_2O_3		RO_2	
MgO	0.190	Al_2O_3	1.248	SiO_2	12.600
SrO	0.095				
BaO	0.095				
CaO	0.610				
Na_2O	0.010				

Steady-State Furnace

Figure 13 is a photograph of the front of the 22" X 10" X 10" furnace. The 6 inch and 8 inch diameter access ports shown in the photograph, as well as a 6 inch diameter access port in the top, were closed with o-ring-sealed plates. The port in the center was a fused quartz window. Figure 13 also shows the flexible bellows servicing the upper diffusion-cell clamp as well as some of the upper heat shielding. Top and bottom clamps consist of opposed slotted rings with tri-position stud holes. Insulating refractories were parted to show one of the asbestos-cloth-wrapped electrical leads bolted to one side of the heating element base. The electrical heating element was a special size SGR SiC Globar unit 2 1/2 inches inside diameter by 8 inches long with a resistance of 1 ohm manufactured by the Carborundum Company, Niagara Falls, New York. This heating element was found to be superior in performance and ease of use to any of several wire-wound heaters.

Figure 14 shows other features of the steady-state furnace in schematic form. The Pt-13% Rh thermocouple positioned just outside the heating element was attached to a Wheelco potentiometer. The temperature of the Pt-13% Rh thermocouple at the diffusion barrier was read by means of a Leeds and Northrup millivolt potentiometer, Catalog No. 8690.

The power control for the heating element was a Powerstat variable transformer, Type 12560 4P, 0 to 280 volts, 112 amps maximum, 31.4 k.v.a. maximum, manufactured by Superior Electric Company, Bristol Connecticut.

Separate Duo Seal vacuum pumps evacuate the furnace proper and the spaces between the two o-rings at each end of the diffusion cell.

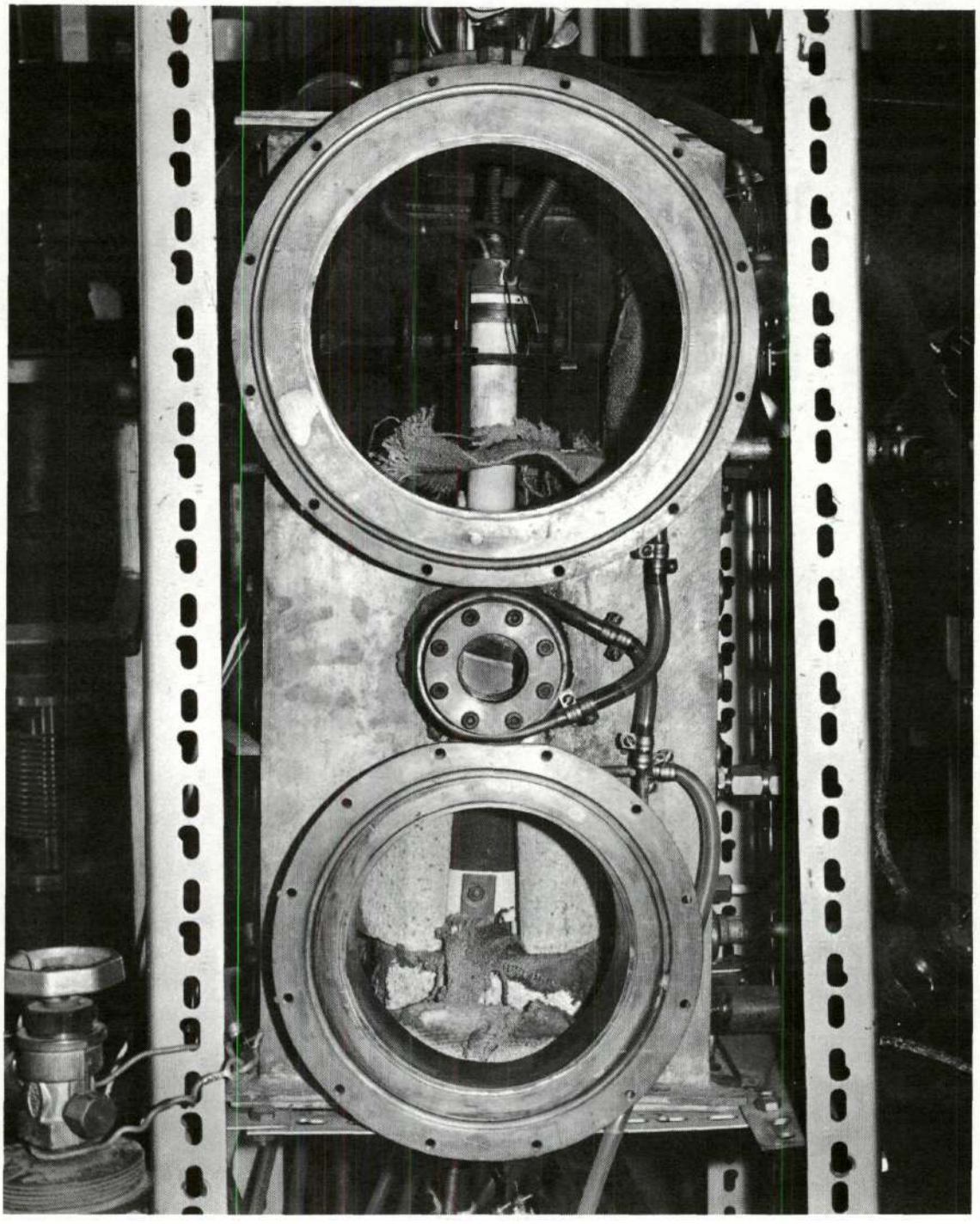

Figure 13. Front of Steady-State Furnace

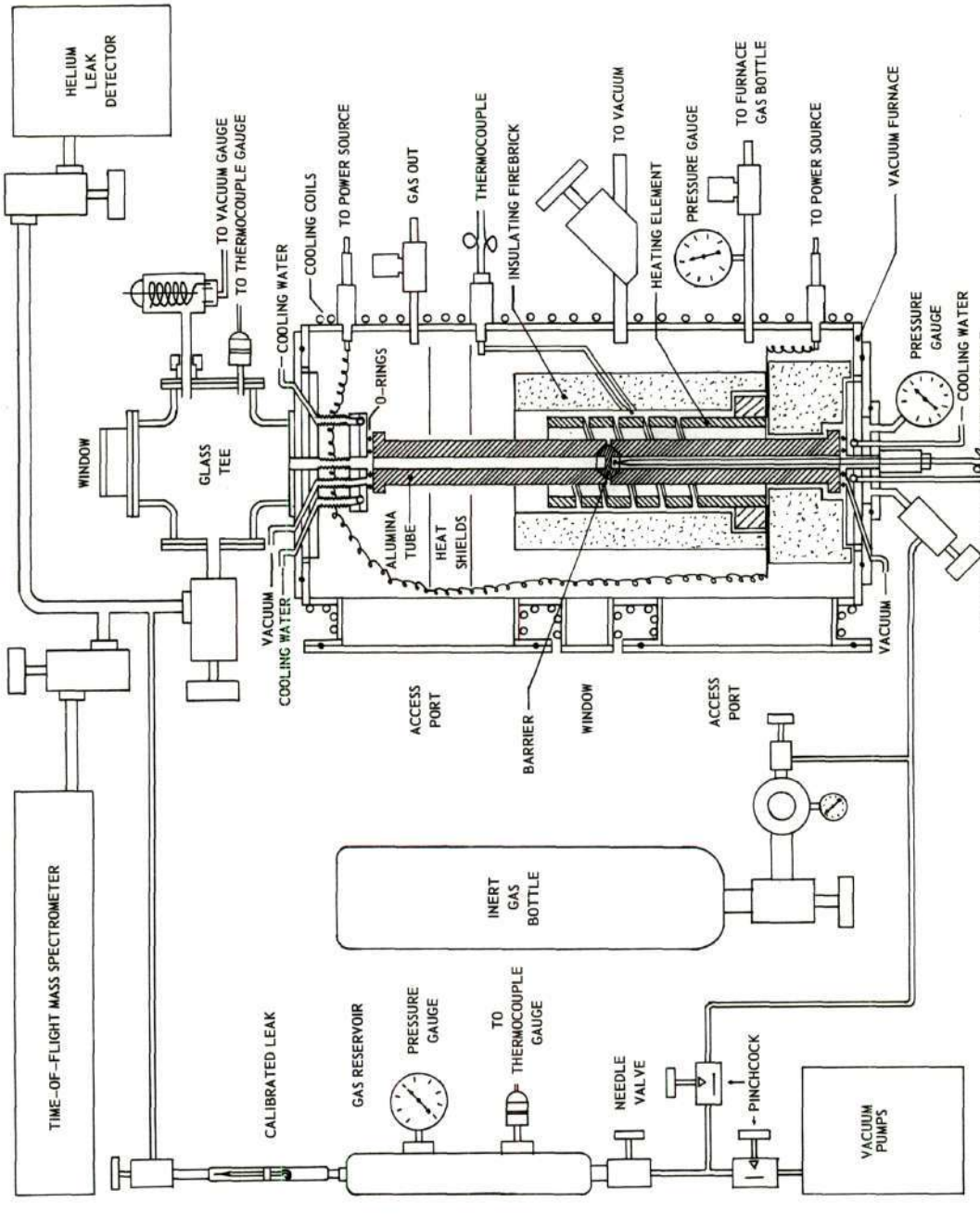

Figure 14. Schematic of Steady-State System

Two valved 1/4-inch pipe ports into the furnace were provided for continuous circulation of any desired gaseous atmosphere.

Conax vacuum-tight electrical lead-throughs were used to admit power and thermocouple wires through the metal wall of the furnace.

Fresh water makes a single circuit through the cooling coils to a drain.

Gas pressure against the lower side of the barrier was measured with a Bourdon-type mechanical gauge mounted on a plate at the bottom of the furnace. This plate, which also holds the barrier-thermocouple lead-through and a vacuum valve, was o-ring sealed to the bottom of the furnace through which a passage lead to the bottom end of the diffusion cell. Pressure at the top end of the diffusion cell was measured with a Veeco thermocouple gauge, Catalog No. DV-IM, and a Veeco R.G. 75K ion gauge mounted to a brass plate which was o-ring sealed to a horizontal arm of the 2-inch glass cross at the top of the furnace.

A 1-1/2 inch diameter fused quartz window in the top vertical arm of the glass cross permitted visual observation of the barrier.

A vacuum valve mounted to a brass plate was o-ring sealed to the other horizontal arm of the glass cross. This permitted isolation of the furnace from the piping leading to the other components of the system.

Non-Steady-State Furnace

Figure 15 shows the equipment used for firing the non-steady-state specimens. The furnace was a water cooled 10" x 10" x 12" box with a 3" inside diameter by 7-1/2" long appendage to the rear which received service connections. The end of the appendage was closed by an o-ring-sealed brass plate. A 6" diameter access hole in the front of the

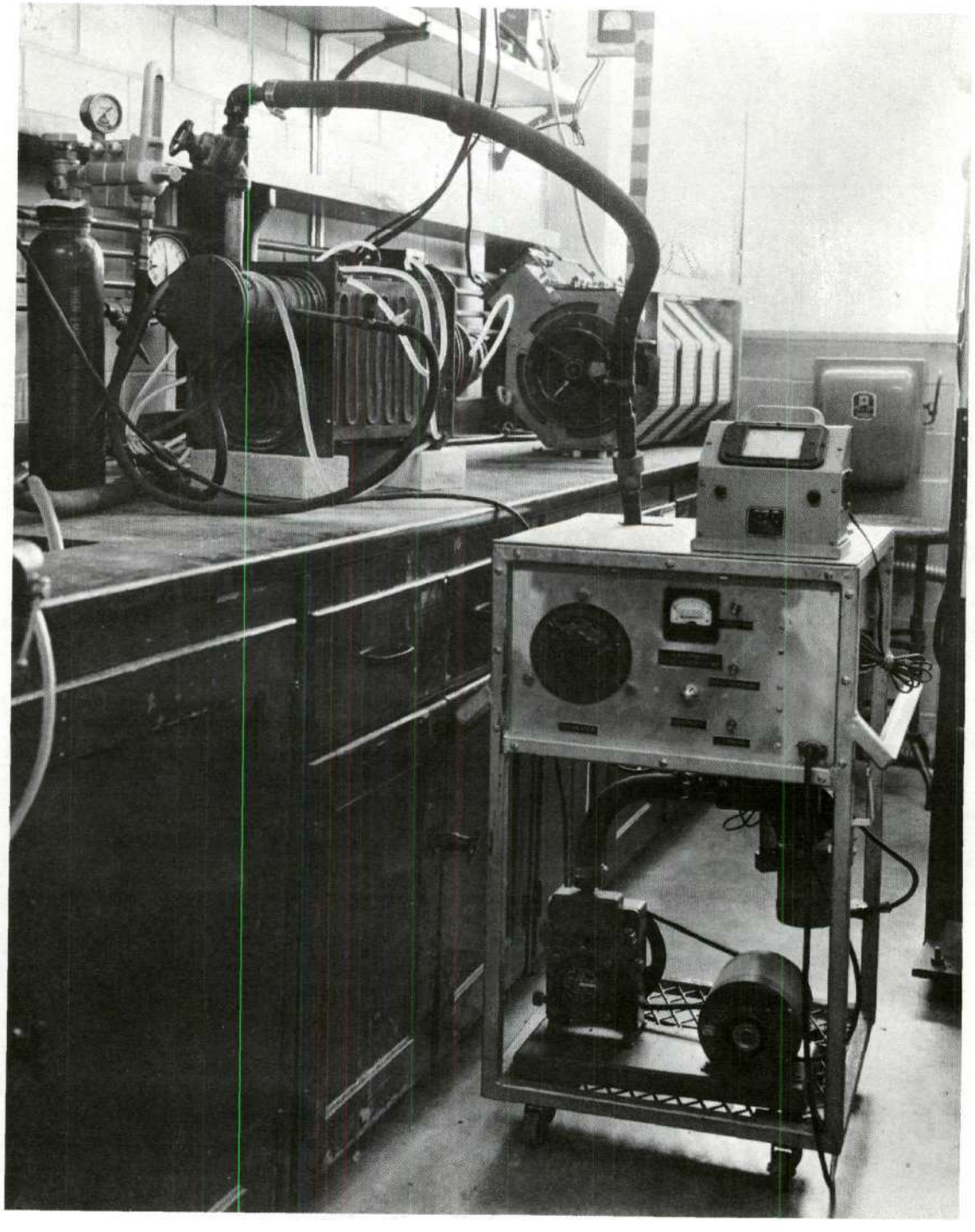

Figure 15. Non-Steady-State Furnace

furnace was o-ring sealed with a brass plate to which was attached a 1 1/2" diameter fused quartz window.

Conax vacuum tight lead-throughs carried power through the metal walls of the appendage to a Globar SGR silicon carbide heating element 1 1/2" inside diameter by 8" long with a resistance of 1/2 ohm. The heating element was supported near the center of the metal box by insulating refractories set on the floor of the box. The power control for the heating element was the same one already described for the steady-state furnace.

Temperature was measured by sighting on the specimen through the fused quartz window with a Pyro optical pyrometer. Furnace pressure was measured with a Bourdon-type pressure gauge mounted in the appendage. A vacuum system consisting of a Veeco oil diffusion pump and a Duo Seal mechanical pump was attached to the appendage via a vacuum valve. The system was equipped with a Veeco thermocouple gauge for low pressure measurement. A valved, 1/4" pipe attached to the appendage admitted gas to the evacuated furnace, and rubber vacuum hose conducted the inert gas from its regulator-equipped storage bottle into the furnace.

Gas Flow Calibration System

It was necessary to design a gas flow calibration system into the measurement apparatus for steady-state flow. The primary purpose of the calibration system was to permit rapid calibration and assignment of gas flow values to correlative areas under curves plotted by the readout equipment of the mass spectrometer. This was necessary because of drift with time and room temperature of mass spectrometer readings.

Figure 14 shows in schematic form the components and their relative positions. The heart of the system was a glass leak made by Robert H. Work, Gibbstown, New Jersey. This leak was calibrated for flow in terms of pressure across the orifice for helium, neon, argon, krypton and xenon gases. The downstream side of the leak lead to a vacuum valve which controlled flow from the leak into the copper piping leading to the mass spectrometer and helium leak detector. The upstream side of the leak was connected to a gas reservoir.

The reservoir, constructed of silver soldered 1 5/8" outside diameter copper tubing and reducer fittings, held the pressure measuring apparatus of the system. A Veeco thermocouple gauge, Catalog No. DV-1M combined with a Heraeus Model 52-220 diaphragm gauge and a Bourdon gauge covered a continuous pressure range of one micron of mercury to fifteen pounds per square inch. A needle valve controlled the inlet of gas into the reservoir.

Upstream from the needle valve was a tee which branched to a vacuum system and the inert gas bottle by way of rubber vacuum tubing. Pinchcocks on the rubber hose controlled flow to the vacuum system and gas bottle.

Mass Spectrometer

A Model 12-101 Bendix Time-of-Flight Mass Spectrometer, equipped with a Model S-14-107 Ion Source and two channel analog output system, was used to sense and measure gas flows in the steady-state diffusion studies. The mass spectrometer and some of its accessory equipment is shown in Figure 16. An extra long flight tube for better resolution was a feature of this model. Another feature was an improved vacuum system

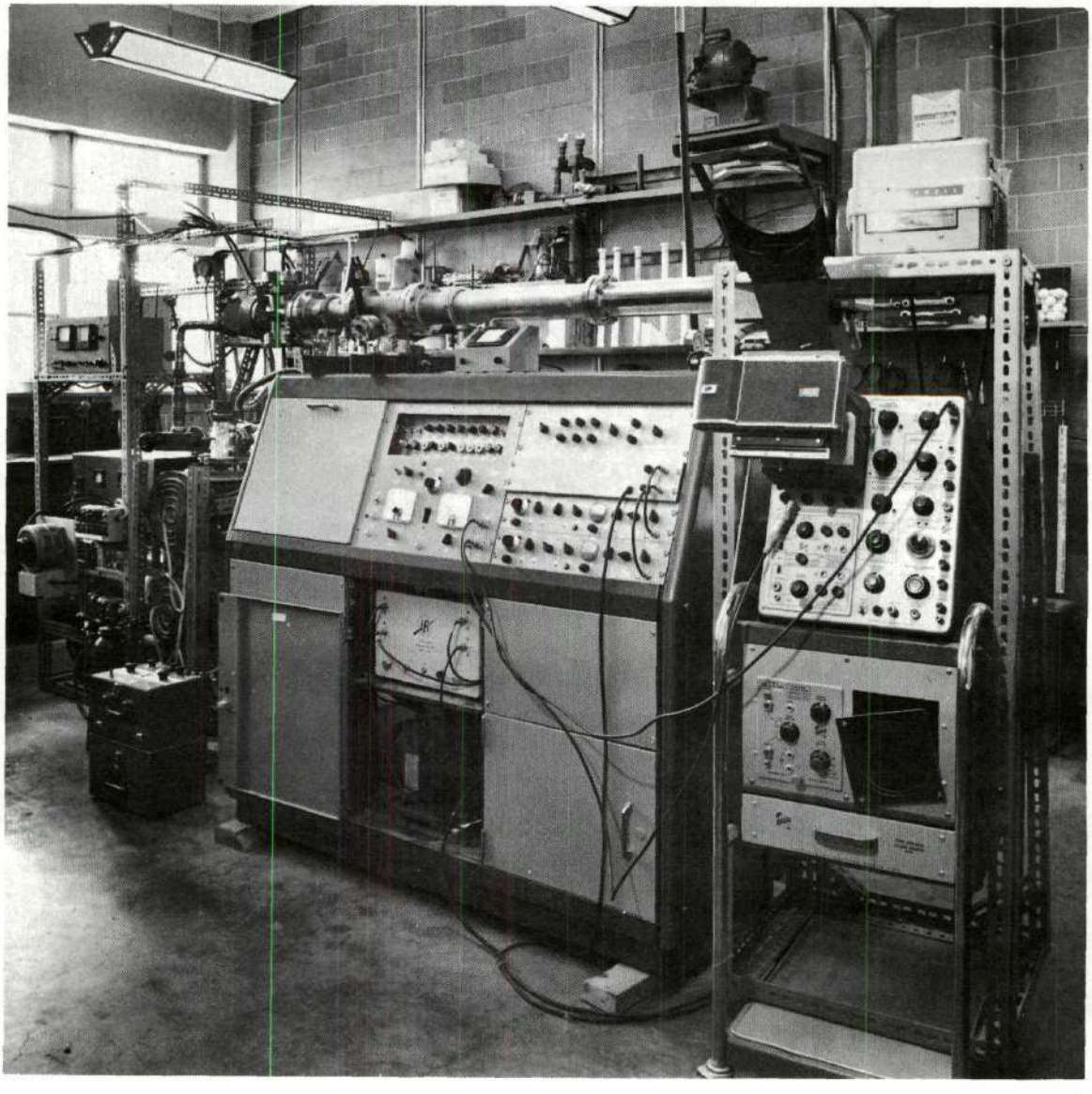

Figure 16. Bendix Time-of-Flight Mass Spectrometer and Accessories

over previous models. It included a Consolidated Vacuum Type MHG-180 Three-Stage Mercury Diffusion Pump attached to a freon-refrigerated cold trap integral with a liquid nitrogen cold trap. In series with this was a Duo Seal mechanical vacuum pump preceded by an activated-alumina-filled filter cartridge. An automatic liquid-nitrogen-trap filler incorporating electrical failure features completed the pumping set up. System pressure in the range 1×10^{-6} millimeters of mercury to atmospheric pressure was measured by a Veeco discharge gauge and a Veeco thermocouple gauge.

A Tektronix Type 543 Oscilloscope System, including a Type CA Two-Channel Preamplifier was used for display of the output of multiplier. A Super Video Wideband Amplifier, Model 395A, manufactured by Instruments for Industry, amplified the signal from the multiplier and fed it to the oscilloscope preamplifier. The oscilloscope was mounted on a Tektronix Type 500/53A Scope-Mobile and was equipped with Tektronix Model C-12 Oscilloscope Camera.

A Model 906 C 159 FGHX Minneapolis-Honeywell Visicorder, equipped to receive four separate analog outputs, produced a plot on photosensitive paper of mass-peak intensity versus scan time.

By means of the mass selector in the analog output section of the mass spectrometer, the individual mass peaks in the spectrum could be picked out and correlated with a number on the selector dial. The dial was scaled in units between 0 and 1000 and controlled the position of a visible gate marker on the oscilloscope trace. The location of any desired mass on the oscilloscope trace or Visicorder plot was determined by use of the relation:

$$P_2 - P_1 = k(\sqrt{2m_2}/e - \sqrt{2m_1}/e) \qquad (13)$$

where P = position of peak

k = a constant

m = atomic mass number

e = ion charge in electrostatic units

The instrument will automatically scan up or down the mass spectrum at any one of nine different scan rates from the point set by the mass selector.

Sensitivity of the analog output electrometer could be selected by means of a decade scale from 0.01 to 1000 millimicroamperes and a scale range selector with multiplying factors of 1, 2 and 4. The analog output section also had a ten-position time constant selector with range from 0.02 to 10 seconds.

Piping System of Steady-State Apparatus

A vacuum-tight copper piping system interconnected the mass spectrometer, diffusion cell, calibrated leak and helium leak detector in the arrangement shown schematically in Figure 14. All permanent connections were silver soldered. All movable connections were o-ring type vacuum quick couplings. All valves were metal-bellows type vacuum valves. Most of these valves and couplings are visible in Figure 17.

A Veeco Model MS-9 helium leak detector was semi-permanently installed in the piping system to detect system leaks and to serve as an auxillary vacuum system. The valve arrangement on the leak detector allowed its use for leak checking other equipment without disconnecting it from the diffusion piping system.

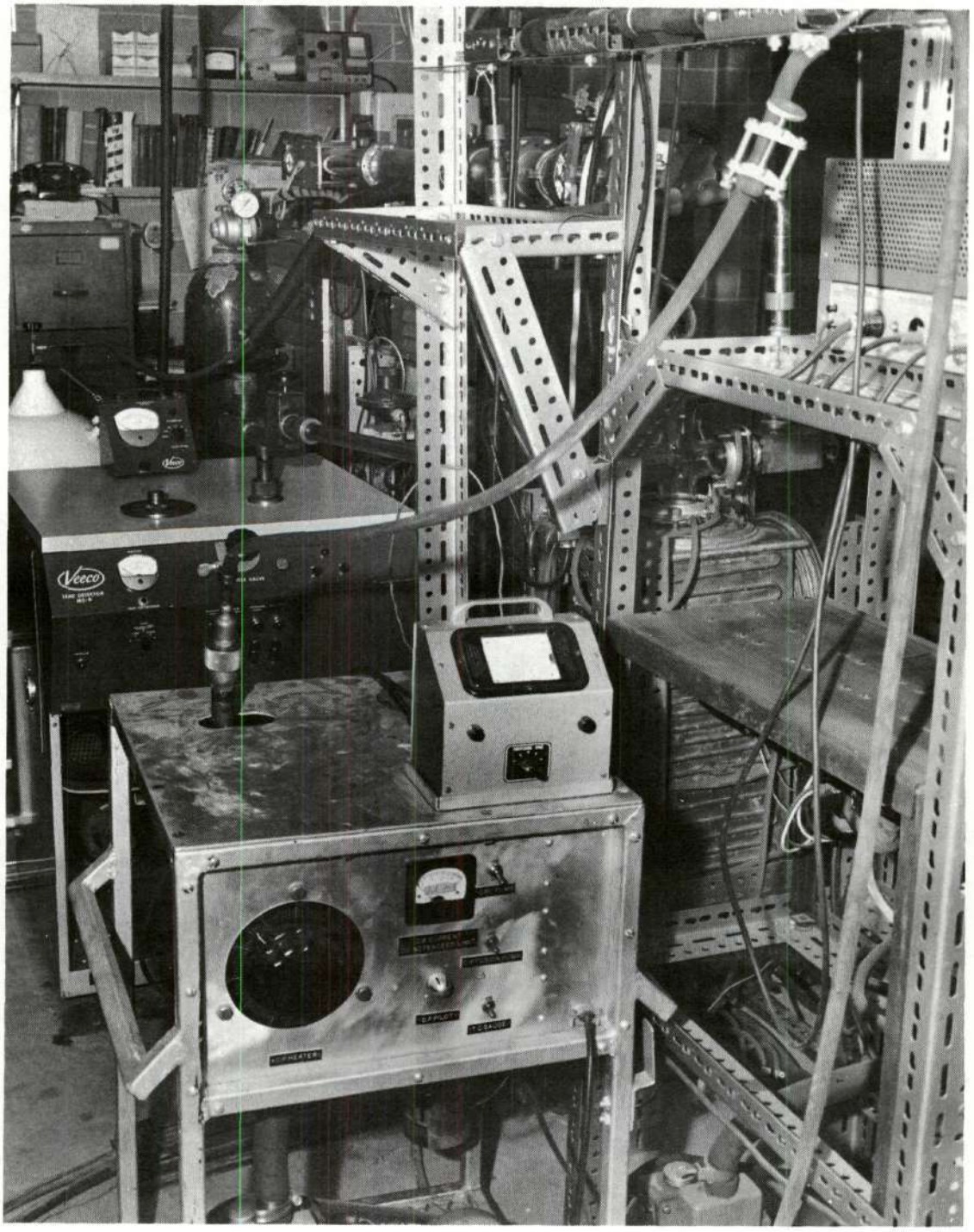

Figure 17. Back View of Steady-State Apparatus

X-Ray Fluorescence Spectrometer

Inert gas gradients in the non-steady-state diffusion samples were investigated with a Norelco Universal Vacuum X-Ray Spectrograph Catalog No. 52360 manufactured by Phillips Electronic Instruments Company, Mount Vernon, New York. This instrument and its accessories are shown in Figure 18. The crystal chamber of this model houses a two-position precision crystal holder and a gas-flow-proportional counter. A lithium fluoride analyzing crystal was used to reflect the characteristic radiation of krypton. A Norelco scintillation device mounted externally to the crystal chamber could also detect the X-rays reflected from the crystal. X-rays were supplied by a Norelco FA 60 X-ray tube with a tungsten target powered by a Norelco Model 12045B3 power supply.

A Norelco Catalog No. 12206 electronic circuit panel received information from the scintillation device into the pulse height analyzer (PHA). The scintillation counter or gas-flow-proportional counter produced output pulses having amplitudes proportional to the krypton characteristic wave lengths received from the analyzing crystal. The function of the PHA was to pass pulses within the amplitude range of interest and to reject pulses of greater or smaller amplitude. The output of the PHA went to the timing, counting and ratemeter circuits which accumulated it in any one of three forms:

A. Counts accumulated during a fixed time interval.

B. Time required to accumulate a fixed number of counts.

C. Instantaneous counting rate.

The accumulated data was read out on a "Servo-Riter" Servo-Potentiometric Recorder made by Texas Instruments, Inc., Houston, Texas.

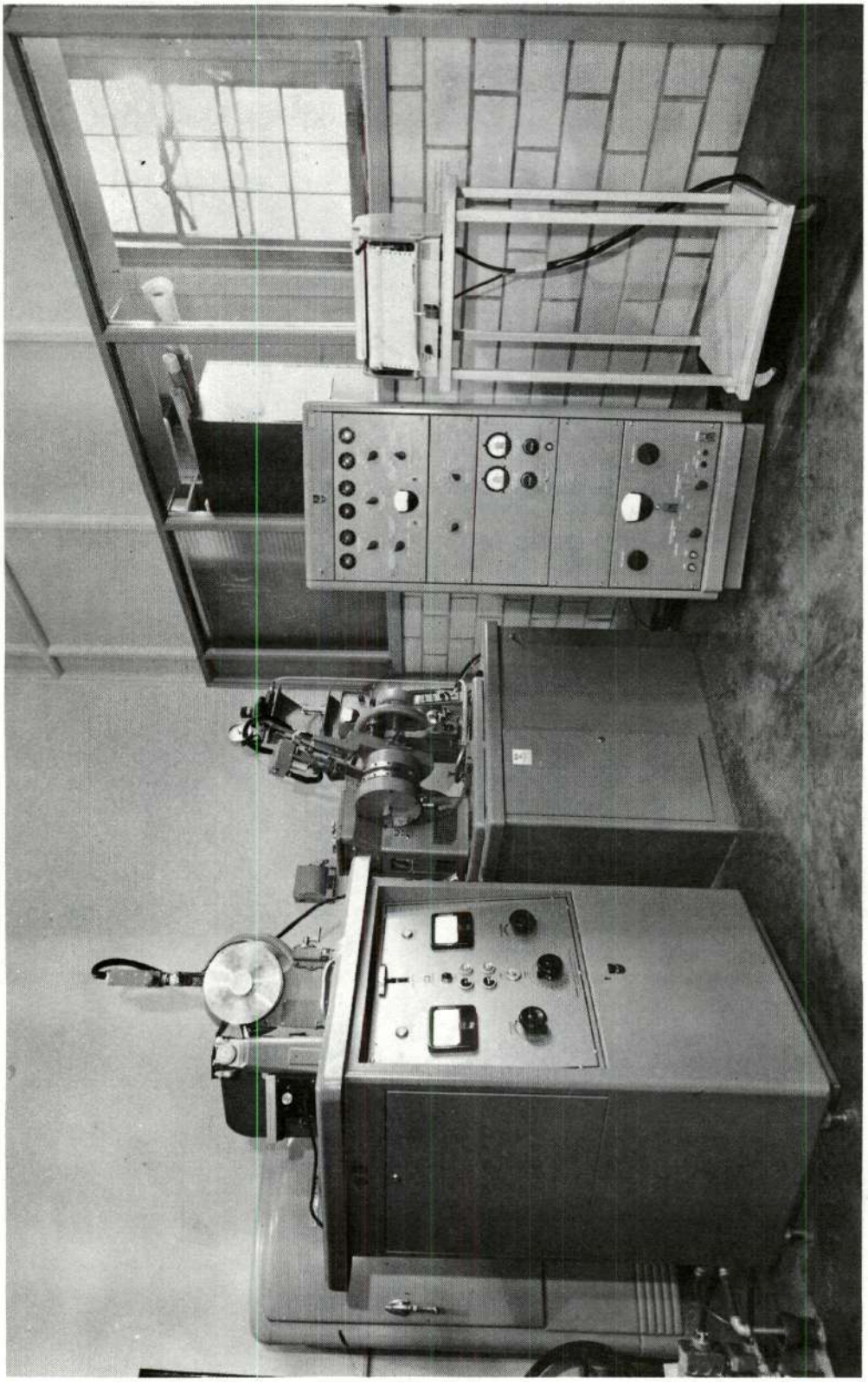

Figure 18. X-Ray Fluorescence Spectrometer

Polar Planimeter

A Compensating Polar Planimeter, Model No. 4236, made by the Keuffel and Esser Company, New York, New York, was used to measure areas under curves plotted by the read-out devices of the steady-state and non-steady-state systems.

CHAPTER IV

EXPERIMENTAL PROCEDURE

Introduction

The experimental procedures for the two methods of studying diffusion employed in this work differed greatly. In the steady-state studies, the equipment for heating the specimen and applying the inert gas to it was connected on stream with the instruments for measuring gas flow. In the non-steady state, the instrumentation for determining gas permeation into the specimen was of necessity detatched from the atmosphere furnace. The steady-state procedure required a great deal of finesse and manipulative skill due to the fragility of the barrier assemblies and the complexity of the instrumentation. The non-steady-state specimens, on the other hand, were rugged and the associated equipment was simple and easy to manipulate. Certainly, the X-ray spectrometer is a complex device; but it was relatively trouble free compared to the time-of-flight mass spectrometer. The operation and calibration procedures of the X-ray spectrometer have been long established, whereas the procedures for use of the mass spectrometer were worked out to a great extent as this research progressed. The details of each procedure are given in separate sections below.

Steady-State Procedure

The steady-state procedure entails the coordination of the three subsystems which make up the steady-state system. They are the furnace

system, the mass spectrometer, and the piping and valve system which includes the calibrated leak.

Operation of the Furnace

The barrier assemblies were bolted into position inside the vacuum furnace as shown in Figure 14. The space connected to the lower side of the barrier, including the leak calibration system, was evacuated and checked for leaks by means of the helium leak detector. This space was then isolated from the vacuum system by an pinchcock and filled to the desired pressure with neon or krypton gas. The space above the barrier was evacuated to a pressure of less than 10^{-5} millimeters of mercury by means of the vacuum system in the helium leak detector. After each initial pumpdown, the complete vacuum system, including barrier seals, was checked for leaks with the helium leak detector to determine if any damage had been done to the barrier assembly during installation and whether all connections were properly tightened. If no leaks were found the access ports in the furnace were closed and the furnace evacuated to approximately 28 inches of mercury.

The furnace was brought up to temperature at a rate of $50^{\circ}C$ per hour by means of a variable transformer.

Determination of Steady-State Flow

After the barrier had reached the desired temperature for each reading it was necessary to establish that steady-state flow through the barrier had been achieved before taking mass spectrometer readings for record. After the initial heat-up of each barrier a series of barrier scans and their respective background scans were taken every two hours

after the first forty-eight hours until the area under each barrier curve, minus the area under its associated background curve, became the same as for the scan preceding it. A similar procedure was used after each temperature change, but only 12 hours were allowed to elapse before the periodic readings began. What is meant by a barrier scan and background scan is covered in detail in a later section.

Determination of Mass Selector Settings

Before the scan of any given peak in the mass spectrum could be accomplished with the mass spectrometer, its position in the spectrum and its mass selector number were located. This was done in the following way:

Step 1. The mass selector was set at 0 and the spectrum was scanned and recorded to beyond the peak for the isotope Hg^{202} before admission of the inert gas whose location was sought. When a good vacuum had been attained in the mass spectrometer, the recorded spectrum normally showed peaks for only those gases found in quantity in air plus peaks for mercury from the diffusion pump and perhaps some peaks from the vacuum grease used in the piping system, or from the oil in the mechanical pump. The peaks for H_2, N, and H_2O vapor were usually present in sufficient quantity to be visible on the oscilloscope. The peaks appearing on the Visicorder plot were marked with their mass numbers. The mass selector was put into manual mode of operation and the dial changed until two separate known peaks had been located via the oscilloscope

and their mass selector numbers recorded. From this data the constant k in Equation 13 was determined.

Step 2. A mass selector number was calculated for each inert gas from Equation 13 using the k value determined above. Both neon and krypton have multiple stable isotopes; therefore, a mass selector number was calculated for the highest and lowest isotope mass for each gas. The mass selector used for the scanning of the peak was set slightly below the low number and the mass selector of the other channel was set slightly above the higher number and left in the manual mode of operation. This made it possible to visually determine when the scan was completed by observation of the oscilloscope. When the scanning gate on the oscilloscope screen was even with the stationary gate, the whole set of peaks of interest had been scanned and a reading thus accomplished.

Step 3. To check the calculated mass selector settings, a sample of each inert gas of interest was introduced directly into the ionization region of the mass spectrometer via a pair of glass petcocks. A strong peak for the gas was displayed on the oscilloscope and Visicorder record. The mass selector was adjusted to the position of the peaks for each inert gas and the number noted. The selector was then tuned to positions immediately before and after the set of peaks and these numbers noted. If these numbers compared favorably with the calculated numbers, they were used to make scans for data.

A scan of the spectrum before and after admission of neon and krypton is shown in Figure 19, along with a detail of the peaks for neon and krypton. Mass selector settings used for neon and krypton are given in Table 5.

Operation of the Valve and Piping System

After steady-state flow was established, a series of mass spectrometer readings were taken to determine the rate of flow of inert gas through the barrier. First, a background reading was made to determine the area under the readout curve not accountable for from the barrier or the leak. Next, the system was isolated from the mass spectrometer, with the exception of the barrier, and a barrier scan was made. The background was subtracted from the area under the curve for the barrier scan to give an area attributable to the flow of gas through the barrier only. Lastly, two or more leak scans and associated background scans were made with two or more different gas pressures against the calibrated leak so as to provide readout areas both above and below the area obtained from the barrier scan. This was the means of linking the flow rate through the barrier with the known flow rates through the calibrated leak. The details of each type of scan or reading, in their proper order, are given below.

After closing the valves to the top of the barrier, the downstream side of the calibrated leak, and the leak detector, the valve to the mass spectrometer was opened. After waiting 5 minutes from the last valve setting, a background scan of the peak for the inert gas in the system was made. The mass spectrometer controls were set as shown in Table 5 for all readings.

Table 5. Mass Spectrometer Settings

Barrier Designation	A (Neon)	A (Krypton)	B (Neon)	B (Krypton)
Electron Energy (volts)	70	70	70	70
Trap Current (microamperes)	0.125	0.125	0.125	0.125
Electrometer (millimicroamperes)	0.01	0.01	0.01	0.01
Scale Factor	1	1	1	1
Scan Rate	3	3	3	3
Time Constant	0.2	0.2	0.2	0.2
Mass Selector Setting	230 to 260	490 to 540	230 to 260	490 to 540
Gate Width	Midrange	Midrange	Midrange	Midrange
Ion Generation	Pulsed +	Pulsed +	Pulsed +	Pulsed +
Electron Beam Generation	Pulsed	Pulsed	Pulsed	Pulsed
High Voltage Control	+ Ions	+ Ions	+ Ions	+ Ions
Visicorder Paper Speed (Inches/Sec.)	0.2	0.2	0.2	0.2

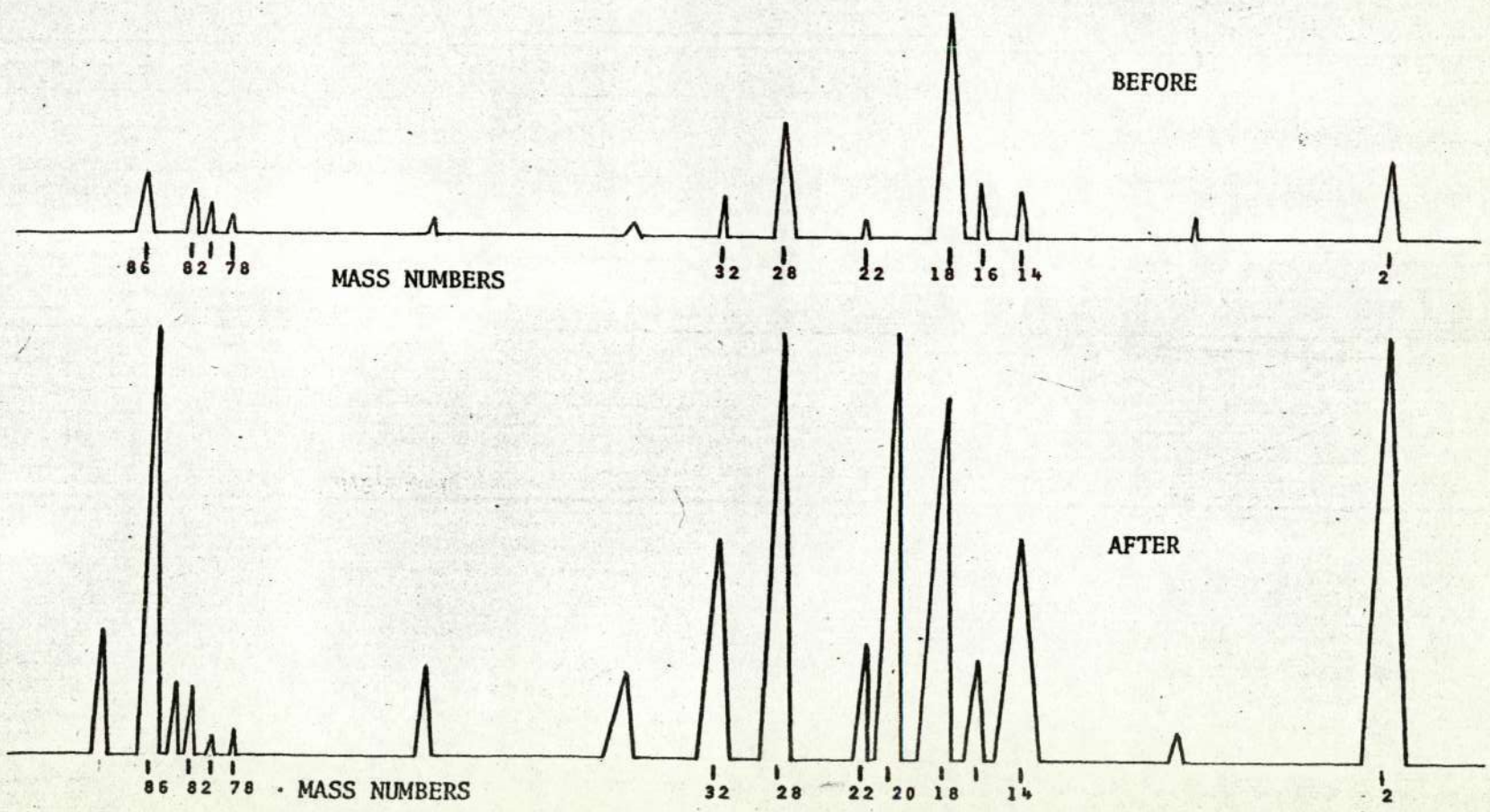

Figure 19. Visicorder Traces Before and After Admission of Neon and Krypton

To set up for the next reading, the barrier scan, the mass spectrometer valve was closed, the leak detector valve opened, and the barrier valve opened. The leak detector valve remained open long enough to pump out the initial surge of gas held behind the barrier valve. The leak detector valve was closed and the mass spectrometer valve opened. Five minutes from the time the mass spectrometer valve was opened, the barrier scan was made with the mass spectrometer. The mass spectrometer valve was then closed, the barrier valve closed, and the leak detector valve opened for five minutes to get ready to make the second background scan.

After the leak detector valve was closed, the mass spectrometer valve was opened and five minutes later the second background scan was made.

At the time the inert gas was admitted to the lower side of the barrier, one atmosphere of the gas was admitted into the evacuated calibrated leak system. In preparation for the first leak scan, the pressure in the leak system was pumped down to an arbitrarily lower level which would be on scale on the mass spectrometer readout, but above the barrier scan in intensity.

Before opening the valve leading from the calibrated leak, the mass spectrometer valve was closed and the barrier valve remained closed. The leak detector valve was opened and then the leak valve was opened. After pumping out the accumulated gas behind the leak valve for five minutes, the leak detector valve was closed and the mass spectrometer valve opened. After five more minutes, the first leak scan was made.

After the first leak scan, a third background scan was made following the same procedure with the leak valve as had been followed with the barrier valve in making the second background scan.

Finally, the pressure in the calibrated leak system was reduced further to an arbitrary level to give a second leak scan intensity, preferably below that of the barrier scan.

The temperature of the barrier was then changed to the next level. When a steady-state of flow through the barrier was obtained, the data-taking procedure above was repeated, and so on, until at least three temperature levels around 100°C apart had been investigated.

Methods of Calculation

The methods and equations employed in calculation of variables and constants are given for each separate variable and constant in the following sections. Sample calculations of each are presented in Appendices A, B, C, and D.

Flux Through the Barrier

Areas under the curves plotted by the Visicorder were measured with a polar planimeter. The differences in areas for the two calibrated leak scans were determined and the difference in the areas for the barrier scan and the smaller calibrated leak scan were found. From these differences an interpolating fraction was formed with the latter difference as numerator and the former difference as denominator. For this interpolating factor to be useful, it was necessary to prove that the relationship between areas under the curves versus pressure against the calibrated leak was linear for Kr and Ne. Figure 20 shows the relationship to be a good approximation of a straight line over a wide pressure variation for both gases.

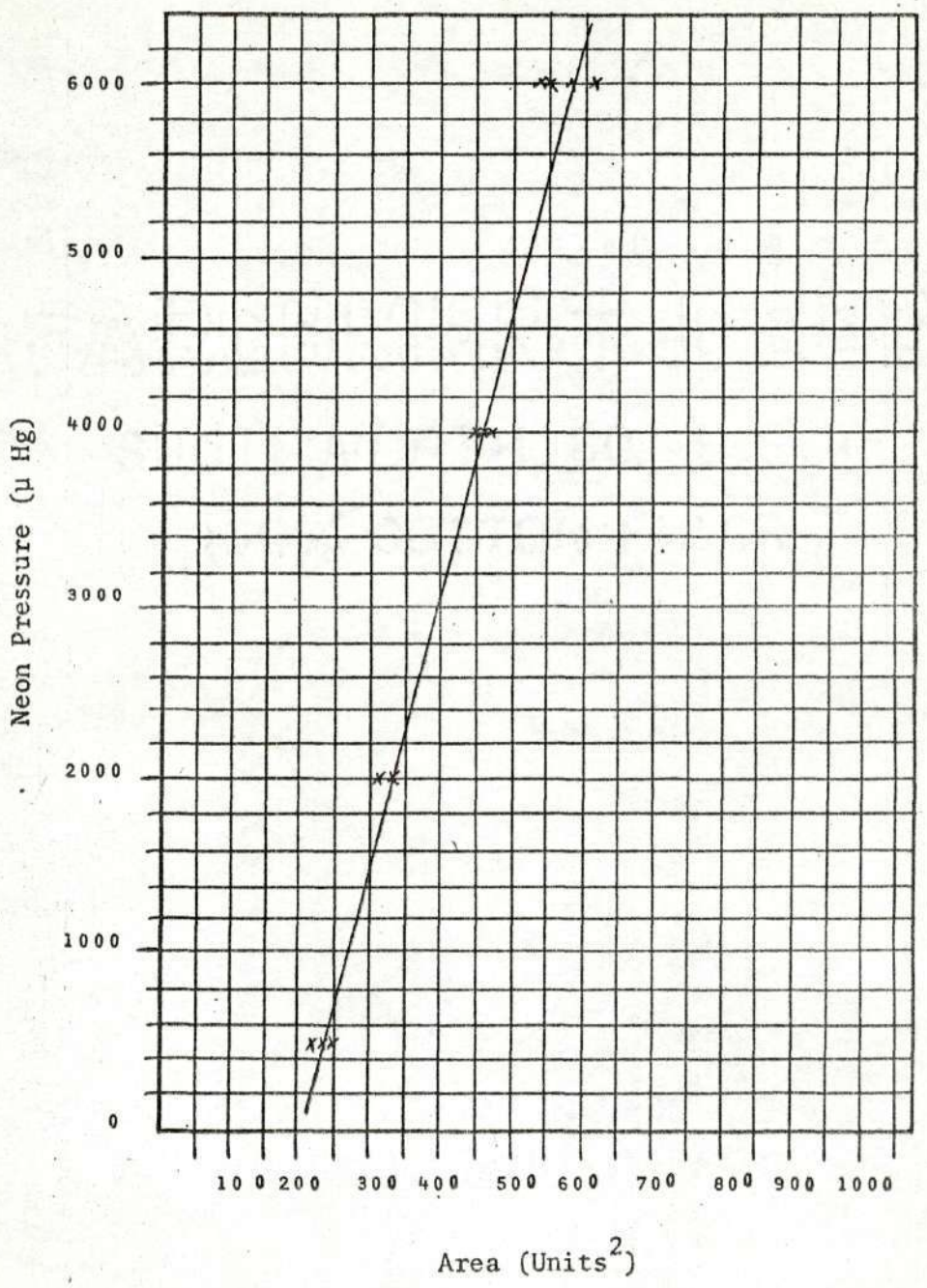

Figure 20. Neon Pressure vs Area Under Curves

It must be understood, however, that the absolute values of the readouts for a given set of gas flow conditions would not necessarily be the same over a long period of time. Sensitivity of the mass spectrometer does vary with such factors as cleanliness of the resistive surfaces of the glass plates in the ion amplifier, condition of source filament, and many other factors involving the electronics, etc. For the span of time involved in taking readings on the diffusion runs for which data was collected, it was easy to check readout calibration by returning to the calibrated leak at one of the previously used pressures and measuring the area of its Visicorder readout. This gave confidence to the final calculated diffusion rates, even though identical leak pressures from other runs might have entirely different readouts.

Figure 21 is a plot of flow rate through the calibrated leak versus pressure of Ne and Kr. This data was furnished by the manufacturer of the calibrated leak. From this data a flow rate in atoms per second was determined for leak scans with areas both above and below that for each barrier scan. The difference in these two flow rates was found and multiplied by the interpolating factor to give the flow rate, or flux J, through the barrier. A sample calculation of J is given in Appendix A.

Inert Gas Concentration Against the Barrier

The concentration C_1 of atoms on the upstream or lower side of the barrier was calculated from the gas law relation:

$$n/V = pN/RT = C_1 \qquad (14)$$

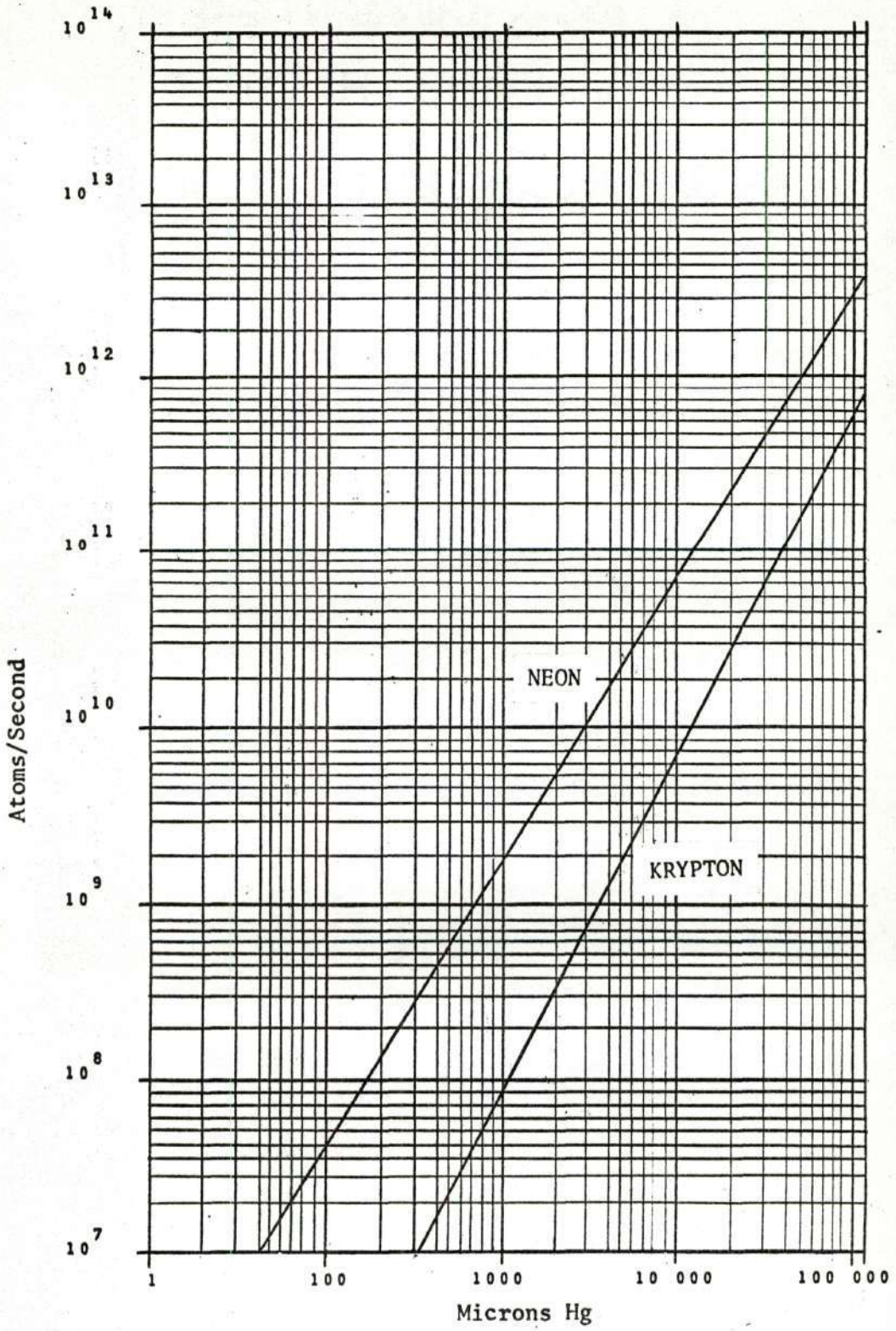

Figure 21. Flow Rate Through Calibrated Leak vs Pressure of Ne and Kr

where n = number of atoms

V = unit volume in cm^3

p = pressure of inert gas against upstream side of barrier in absolute atmospheres

R = gas constant in liter atoms per mole degree

T = temperature of barrier in degrees Kelvin

N = Avogadro's number

The concentration thus determined was in units of atoms per cubic centimeter. A sample calculation with Equation 14 is given in Appendix B.

Diffusion Coefficient

The diffusion coefficient, D, was calculated from the relation:

$$D = \frac{J\ L\ V}{\Delta t\ (A(C_1 - C_2)} \qquad (15)$$

where J = flux through the barrier in atoms per second

L = thickness of barrier in cm

V = unit volume (1 cm^3)

Δt = unit time (1 second)

A = area of barrier in cm^2

C_1 = concentration of atoms per unit volume on upstream side of barrier

C_2 = concentration of atoms on downstream side of barrier (taken as equal to zero)

The D values thus determined are in units of cm^2 per second. A sample calculation using Equation 15 is shown in Appendix C.

Activation Energy

The activation energy E_a was determined for single crystal alumina and polycrystalline alumina by use of the equation:

$$\ln D = \ln D_o - E_a/k\ (1/T) \tag{16}$$

by forming two equations in two unknowns:

$$\ln D_1 = \ln D_o - E_a/k\ (1/T_1) \tag{17}$$

$$\ln D_2 = \ln D_o - E_a/k\ (1/T_2) \tag{18}$$

and substracting Equation 18 from Equation 17:

$$\ln \frac{D_1}{D_2} = - \frac{E_a\ (T_2 - T_1)}{k\ T_1 T_2} \tag{19}$$

Equation 19 is solved for E_a by substituting the D and T values from two points on the D versus 1/T curve. A sample calculation of E_a using Equation 19 is given in Appendix C.

Diffusion Constant

Equation 11 was rearranged to give:

$$\ln D_o = \ln D + E_a/k\ (1/T) \tag{20}$$

for calculation of D_o, the diffusion constant. A sample calculation, using Equation 20, is shown in Appendix C.

Non-Steady-State Procedure

It was desired to make diffusion determinations by an additional method to the steady-state method already described. Availability of good quality equipment for X-ray fluorescence spectrometry presented a possible alternate method. Samples of the single crystal and polycrystalline materials already described were heated in the non-steady-state furnace shown in Figure 15 and held at constant temperature in an atmosphere of inert gas for the desired time. After cooling to room temperature, the samples were submitted to X-ray fluorescence spectrometry to determine the quantity of inert gas captured in the surface of the specimen during heat treatment. A thin layer of the material was then removed from the surface of the specimen by diamond grinding and another quantitative determination of the inert gas made. This procedure was repeated several times to obtain the concentration gradient of the inert gas in the specimen. This procedure was attempted for the determination of krypton only since the mass of neon was too low to be detected by the available X-ray fluorescence spectrometer.

Operation of the Non-Steady-State Furnace

The single and polycrystalline specimens were loaded into the non-steady-state furnace already described and the furnace was evacuated to around 28 inches of mercury. The temperature of the specimens was slowly advanced to 2000^{o}F by means of a variable transformer. Krypton gas was admitted to the furnace to a pressure of one atmosphere. The atmospheric conditions of 2000^{o}F and one atmosphere of krypton gas were maintained for 156 hours, at which time the furnace power was turned off.

The specimens cooled to room temperature within two hours while the pressure of krypton gas was maintained at one atmosphere.

Operation of the X-Ray Fluorescence Spectrometer

A sample of the krypton was collected in a small rubber balloon and placed in a sample holder of the spectrometer. The position of two-theta of the K-alpha peak for krypton was determined from tables to be 28.28°. A scan of the krypton filled balloon gave a very strong peak at this position. Using this same known sample and two-theta position a PHA scan was made to determine the settings to give optimum sensitivity to the characteristic K-alpha radiations of krypton. The polycrystalline and single crystal samples which had been heated to $2000^{\circ}F$ and exposed to one atmospheric pressure of krypton for 156 hours were loaded into two of the four sample holders in the spectrometer. Untreated blanks of each type of sample were loaded into the other two sample positions. The sample chamber was evacuated to minimize scattering of X-rays by air. The settings of the X-ray machine and its accessories are listed in Table 6. The gas flow proportional counter was used to scan each specimen in the two-theta range of 27.5° to 28.5° at a rate of $1/8^{\circ}$ per minute. A lithium fluoride analyzing crystal was employed.

Method of Calculation of Non-Steady-State Diffusion

Values for the concentration function $(C_x - C_o)/(C_s - C_o)$ from Equation 8 were to be obtained by measuring the areas under the curves plotted by the X-ray fluorescence equipment. This was to be done by forming ratios of the areas for the concentration at incremental X depths beneath the surface of the specimen to the area for the original

Table 6. X-Ray Fluorescence Spectrometer Settings

X-Ray Generator:		55 KV, 30 MA
X-Ray Fluorescence:	Counter	Gas Flow Proportional
	Analyzing Crystal	LiF
	Sample Chamber	Vacuum
Goniometer:	Scan Rate	$1/8^{o}$ per minute
	Starting Position	27.5^{o}
Counting Circuits	Function Selector	Continuous
	Rate	100 full scale
	Time Constant	1 second
	# 1 Detector	0.7
	# 2 Detector	1.4
P.H.A.	W	12 Volts
	L	22 Volts

concentration at X = 0 beneath the surface. From the relationship between the concentration function and $X/\sqrt{DT}$ given in Figure 4 values of D were to be calculated.

CHAPTER V

RESULTS

Table 7 gives a description of the barriers yielding useful results. Table 8 lists the data gathered from the steady-state experiments. Table 9 gives the values calculated from the data. A plot of diffusion coefficient versus the reciprocal of the absolute temperature is shown in Figure 22.

No useful data was obtained from the experiments aimed at determining activation energy for diffusion of krypton in sapphire and polycrystalline alpha alumina by the non-steady-state technique already described. Apparently, the X-ray fluorescence spectrometer employed in this experiment was of insufficient sensitivity to quantitatively determine the minute amounts of Kr present in the small specimens of alumina available for this study.

Table 7. Description of Steady-State Specimens

Specimen	Type	Barrier Thickness (cm)	Barrier Diameter (cm)	Barrier Area (cm^2)	Density (gm/cm^3)	Gases Applied
A	Single Crystal	.231	.635	.317	4.01	Ne and Kr
B	Polycrystalline	.208	.635	.317	3.89	Ne and Kr

Table 8. Experimental Data For Steady-State Diffusion (Continued)

Diffusion Gas	Neon		
Barrier Designation	Polycrystalline		
Barrier Temperature (°K)	1248	1361	1466
Inert Gas Pressure on Barrier (Atmosphere)	1.0	1.0	1.0
Concentration of Inert Gas Against Barrier (Atoms/cc)	5.88×10^{18}	5.4×10^{18}	5.01×10^{18}
Pressure Across Calibrated Leak (Microns of Hg)			
Low	1000	1000	1000
High	4000	4000	4000
Flow Rates Through Calibrated Leak (Atoms/Second)			
Low	1.9×10^{9}	1.9×10^{9}	1.9×10^{9}
High	1.8×10^{10}	1.8×10^{10}	1.8 C 10^{10}
Areas Under Visicorder Curves Adjusted for Background ($Units^2$)			
Barrier Scan	21	24	27
Low Leak Scan	19	19	19
High Leak Scan	37	37	37
Area Factors for Calculation of Barrier Flow Rates (No Units)	2/18	5/18	8/18
Flow Rates Through Barriers			
J (Atoms/Second)	3.8×10^{9}	6.37×10^{9}	9.06×10^{9}

Table 8. Experimental Data for Steady-State Diffusion (Continued)

Diffusion Gas	Neon		
Barrier Designation	Single Crystal		
Barrier Temperature (^{o}K)	1223	1288	1436
Inert Gas Pressure on Barrier (Atmosphere)	1.0	1.0	1.0
Concentration of Inert Gas Against Barrier (Atoms/cc)	6.0×10^{18}	5.7×10^{18}	5.1×10^{18}
Pressure Across Calibrated Leak (Microns of Hg)			
Low	4000	5000	5000
High	6000	8000	15000
Flow Rates Through Calibrated Leak (Atoms/Second)			
Low	1.55×10^{12}	2.24×10^{12}	2.24×10^{12}
High	3.00×10^{12}	4.8×10^{12}	1.3×10^{13}
Areas Under Visicorder Curves Adjusted for Background (Units^{2})			
Barrier Scan	63	57	31
Low Leak Scan	29	35	26
High Leak Scan	82	100	78
Area Factors for Calculation of Barrier Flow Rates (No Units)	34/53	22/65	5/32
Flow Rates Through Barriers			
J (Atoms/Second)	2.48×10^{12}	3.11×10^{12}	3.27×10^{12}

Table 8. Experimental Data For Steady-State Diffusion (Continued)

Diffusion Gas	Krypton		
Barrier Designation	Polycrystalline		
Barrier Temperature (^{o}K)	1279	1385	1489
Inert Gas Pressure on Barrier (Atmosphere)	1.68	1.68	1.68
Concentration of Inert Gas Against Barrier (Atoms/cc)	9.15×10^{18}	8.92×10^{18}	8.28×10^{18}
Pressure Across Calibrated Leak (Microns of Hg)			
Low	500	500	500
High	1000	1000	1000
Flow Rates Through Calibrated Leak (Atoms/Second)			
Low	2.4×10^{7}	2.4×10^{7}	2.4×10^{7}
High	9.2×10^{7}	9.2×10^{7}	9.2×10^{7}
Areas Under Visicorder Curves Adjusted for Background (Units^{2})			
Barrier Scan	56	71	109
Low Leak Scan	51	51	51
High Leak Scan	114	114	114
Area Factors for Calculation of Barrier Flow Rates (No Units)	5/63	20/63	58/63
Flow Rates Through Barriers			
J (Atoms/Second)	2.94×10^{7}	4.56×10^{7}	8.67×10^{7}

Table 8. Experimental Data for Steady-State Diffusion

Diffusion Gas	Krypton		
Barrier Designation	Single Crystal		
Barrier Temperature (^{o}K)	1249	1398	1483
Inert Gas Pressure on Barrier (Atmosphere)	1.61	1.68	1.49
Concentration of Inert Gas Against Barrier (Atoms/cc)	9.47×10^{17}	8.82×10^{17}	7.38×10^{17}
Pressure Across Calibrated Leak (Microns of Hg)			
Low	500	500	500
High	1000	1000	1000
Flow Rates Through Calibrated Leak (Atoms/Second)			
Low	2.4×10^{7}	2.4×10^{7}	2.4×10^{7}
High	9.2×10^{7}	9.2×10^{7}	9.2×10^{7}
Areas Under Visicorder Curves Adjusted for Background ($Units^{2}$)			
Barrier Scan	42	67	104
Low Leak Scan	60	60	60
High Leak Scan	318	318	318
Area Factors for Calculation of Barrier Flow Rates (No Units)	42/258	67/258	104/258
Flow Rates Through Barriers			
J (Atoms/Second)	3.51×10^{7}	4.17×10^{7}	5.04×10^{7}

Table 9. Calculated Steady-State Diffusion Values

Barrier Designation	Temperature ^{o}C	Diffusion Coefficient, D $cm^2/second$	$1/T^{o}C \times 10^3$	Activation Energy, E_a Electron Volts	Diffusion Constant, D_o $cm^2/second$
Polycrystalline (Neon)	975	4.23×10^{-10}	1.027	0.73	3.82×10^{-7}
	1088	7.74×10^{-10}	0.918		
	1193	1.19×10^{-9}	0.838		
Polycrystalline (Krypton)	1006	1.93×10^{-12}	0.994	1.02	1.91×10^{-8}
	1112	3.36×10^{-12}	0.900		
	1216	6.87×10^{-12}	0.823		
Single Crystal (Neon)	950	3.01×10^{-7}	1.052	0.33	7.70×10^{-6}
	1015	3.97×10^{-7}	0.984		
	1160	4.67×10^{-7}	0.862		
Single Crystal (Krypton)	976	2.70×10^{-11}	1.025	0.41	1.2×10^{-9}
	1125	3.45×10^{-11}	0.888		
	1210	4.98×10^{-11}	0.827		

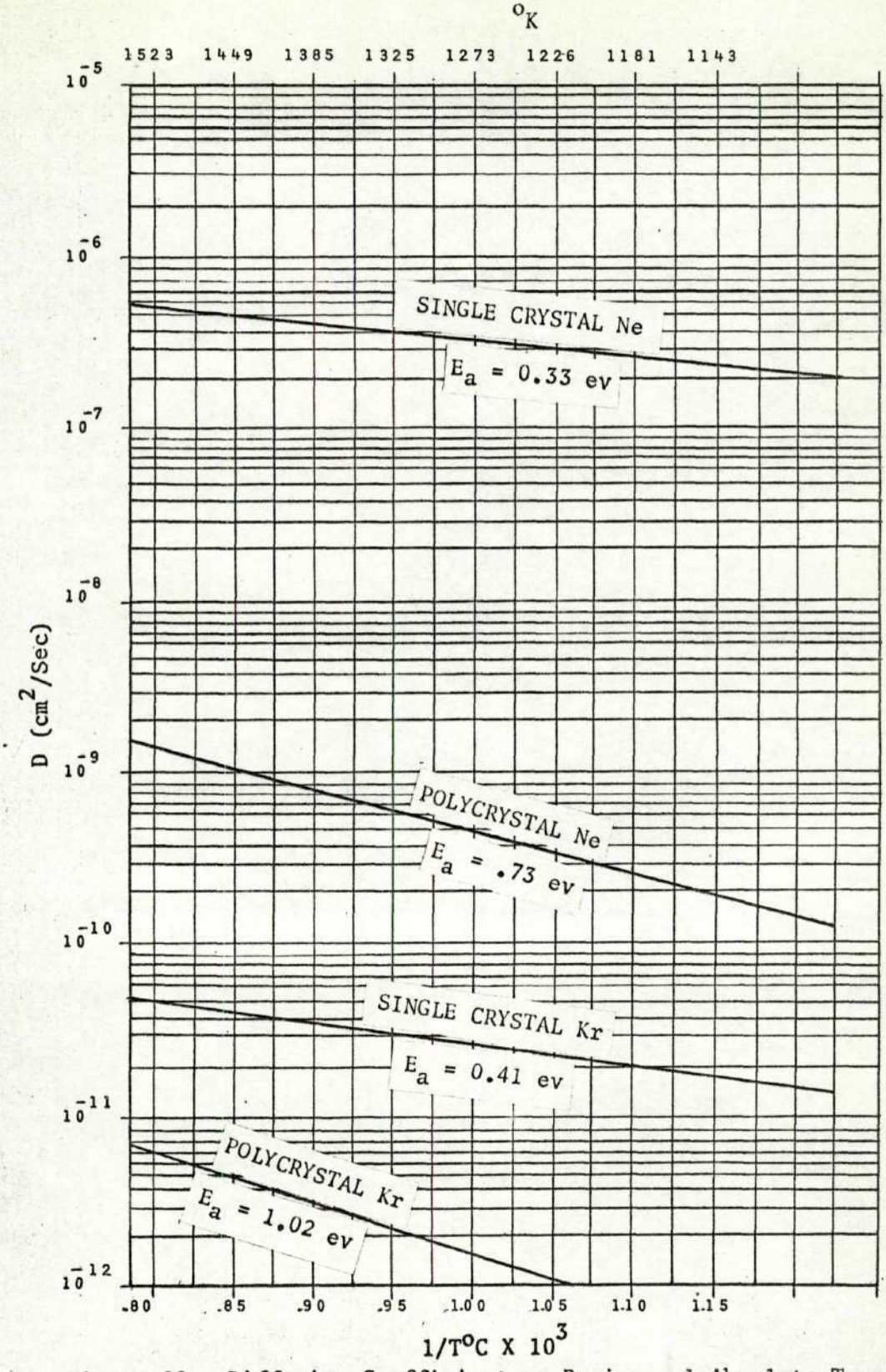

Figure 22. Diffusion Coefficient vs Reciprocal Absolute Temperature

CHAPTER VI

DISCUSSION AND CONCLUSIONS

A comparison of the experimental results in Table 8 with the calculated theoretical values found in Table 10, Appendix D, allows one to draw some conclusions concerning possible mechanisms for the diffusion observed in the experimental work. The theoretical activation energy for diffusion of neon through alumina by the vacancy mechanism was 69.5 electron volts. The theoretical value for krypton diffusion was roughly one order of magnitude higher at 663 electron volts. The experimental value for transport of neon through single crystal alpha alumina was 0.33 electron volts. The value for krypton transport was 0.41 electron volts. Since the theoretical values were greater than the experimental values in both cases by more than two orders of magnitude, it is unlikely that the vacancy mechanism was significant in the transport process observed in the experiments. For the edge dislocation mechanism the theoretical activation energy for diffusion of neon was 2.94 electron volts. This same process for krypton was 376 electron volts. Since the theoretical value of 2.94 electron volts was within one order of magnitude of the experimental value of 0.33 electron volts, the edge dislocation mechanism was probably highly significant in the transport of neon through the single crystal. The experimental value of 0.41 electron volts was less than the theoretical result of 376 electron volts by around two orders of magnitude, making the edge dislocation an unlikely means of

krypton transport.

Experimental activation energy for transport of neon through polycrystalline alumina was 0.73 electron volts. This value compared favorably with the theoretical activation energy at an edge dislocation, making edge dislocation diffusion a probable means of some portion of the neon transport in the polycrystalline alumina specimen. Vacancy defects were ruled out as a means of neon transport in polycrystalline alumina for the same reason given for single crystal alumina. Grain boundary diffusion is usually a significant factor in any diffusion process in a polycrystalline ceramic. Experimental activation energy for transport of krypton through polycrystalline alumina was 1.02 electron volts. Theory predicted 376 electron volts for edge dislocation diffusion and 663 electron volts for vacancy diffusion. The theoretical values for both types of defects were too high to be given serious consideration as the means of krypton transport.

Theory predicted approximately one order of magnitude difference in the activation energies for neon and krypton for both the vacancy and the edge dislocation. Experimental results showed them to be of the same order of magnitude. This leads one to suspect that the diffusion of krypton was assisted by other processes than the simple defect diffusion mechanisms already described. Twins and screw dislocations are possible mechanisms. The work of Selig, Malm, and Claasen[24] has raised the possibility that certain unstable compounds may be formed at reasonably low activation energies between the heavier noble gases and other substances. Some such synergism between krypton and alumina could have contributed to the transport of krypton. Such reactivity between krypton and alumina would be en-

hanced if stresses existed in the alumina specimens. Such stresses were not unexpected since the barrier portions of the specimens were formed by ultrasonic impact grinding. There is also the possibility that the boron carbide used for grinding was impacted into the surface of the barrier and was not completely removed in the subsequent cleaning operations resulting in an increased affinity for krypton in the barrier.

A recent paper by Rama and Hart[36] gave experimental evidence that some degree of isotopic fractionation takes place during the diffusion of neon through Vicor glass. The experiment showed that the diffusion rate of Ne^{20} is greater than that for Ne^{22} by the amount predicted by simple diffusion theory. Although it was not a planned purpose of the present work to determine fractionation of the isotopes of neon and krypton during their transport through alumina, some interesting observations were made in regard to this related subject. Figure 23 shows scale copies of curves obtained from the mass spectrometer readout for the two most abundant isotopes of neon and the four most prevalent isotopes of krypton, both before diffusion through polycrystalline alumina and afterward. The curves clearly show that in the case of both groups of isotopes, the isotopes with the lower masses are diffused at a higher rate than the heavier nuclides with the same atomic number. Quantitative evaluation of this phenomenon was not attempted. This problem should make an interesting topic for investigation at some future date.

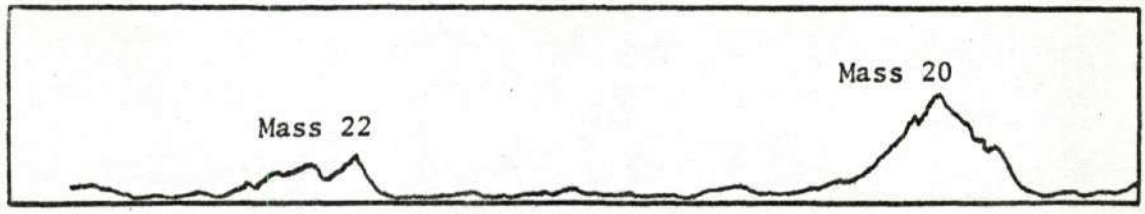

Before Diffusion

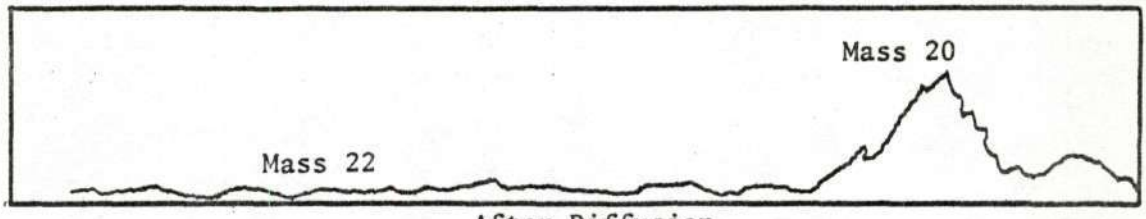

After Diffusion

NEON MASS SPECTRUM

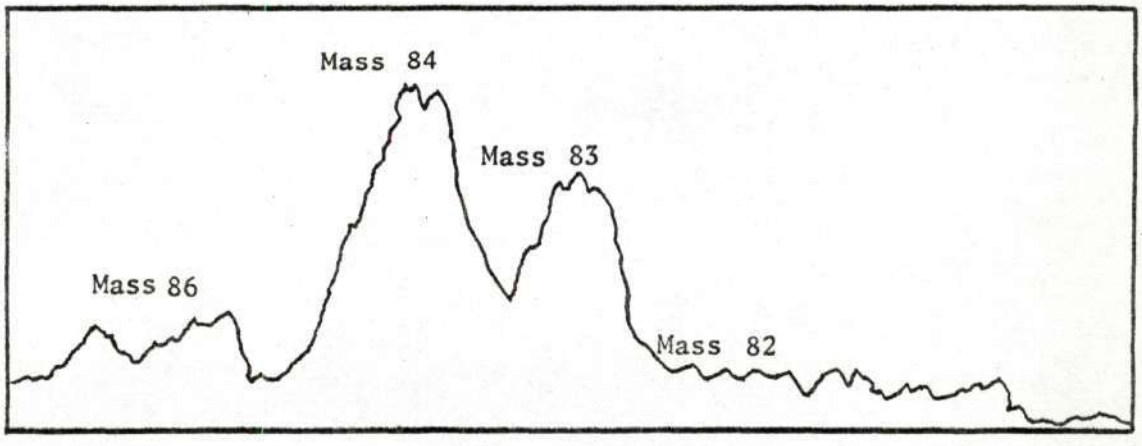

Before Diffusion

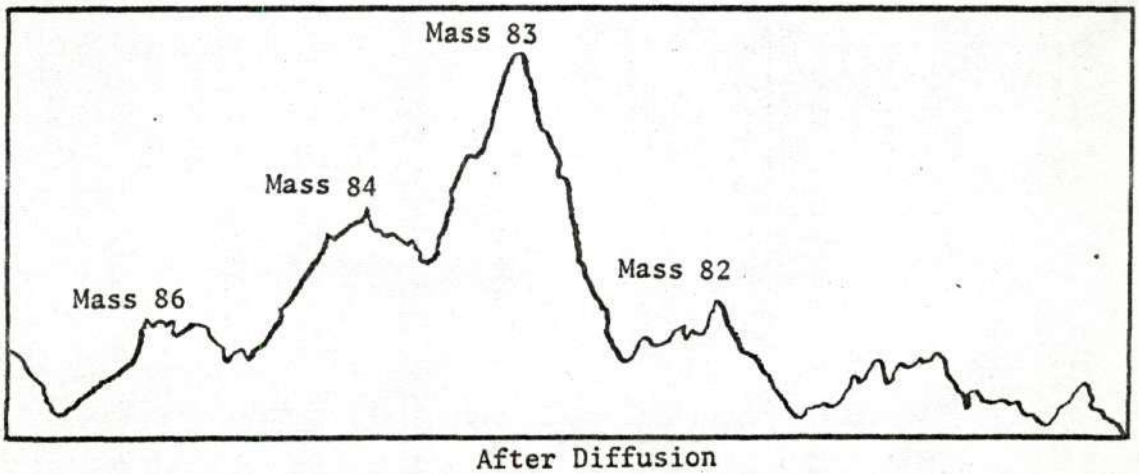

After Diffusion

KRYPTON MASS SPECTRUM

Figure 23. Visicorder Traces for Neon and Krypton Before and After Diffusion

APPENDIX A

Sample Calculation of Flux Through Barrier

Figure 21 shows that a pressure of 1000 microns Hg of Kr against the upstream side of the calibrated leak produced a flux of 9.2×10^7 atoms of Kr per second into the mass spectrometer. The area under the curve plotted by the readout device for that flux, minus the area for Kr background before the flux was introduced, was 318 square units. In like manner, a pressure of 500 microns Hg of Kr, giving a flux of 2.4×10^7 atoms per second, contributed an area of 60 square units. The difference in flux from the two gas pressures was thus $9.2 \times 10^7 - 2.4 \times 10^7 = 6.8 \times 10^7$ atoms per second. The difference in readout areas contributed by the two fluxes was 318 - 60 = 258 square units.

The Kr flux through a single crystal alumina barrier .231 cm thick and .316 cm^2 in area gave a readout area minus background of 102 square units. Taking the difference between the area for the smaller leak rate, 60 square units, and that for the barrier diffusion, 102 square units, gave 42 square units. Since the total difference in area units between the high and low leak rate was 258 square units, and since this represented a difference in flux of 6.8×10^7 atoms per second, this meant that the flux through the barrier at 976°C was $42/258 \times 6.8 \times 10^7 = 1.1 \times 10^7$ atoms per second more than for the lower leak rate. This gave $2.4 \times 10^7 + 1.1 \times 10^7 = 3.5 \times 10^7$ atoms per second as the flux through the barrier, J, at 976°C (1249°K).

APPENDIX B

Sample Calculation of Concentration of Atoms of Inert Gas Against Upstream Side of Steady-State Barrier.

The concentration, C_1, of atoms on the upstream or high pressure side of the barrier was calculated from the gas law relation:

$$n/V = pN/RT = C_1 \tag{14}$$

where n = (to be calculated) = number of atoms

p = 1.61 atmospheres = pressure of inert gas on upstream side of barrier

R = 8.208×10^{-2} = gas constant in liter atmospheres per mole degree K

T = 1.249×10^3 °K = temperature of gas at barrier

N = 6.024×10^{23} = Avogadro's number in molecules/gram mole

V = 1 cm^3 = unit volume

$$C_1 = \frac{1.61 \times 6.024 \times 10^{23}}{8.205 \times 10^{-2} \times 1.249 \times 10^3} = .947 \times 10^{22} \text{ atoms/l} = 9.47 \times 10^{17} \text{ atoms/cm}^3$$

APPENDIX C

Sample Calculation of Diffusion Coefficient, Activation Energy and Diffusion Constant for Steady-State Diffusion of Krypton through Single Crystal Alumina.

The diffusion coefficient, D, was calculated from the relation:

$$D = \frac{J\ L\ V}{A(C_1 - C_2)} \tag{15}$$

where $J = 3.5 \times 10^{7}$ atoms/sec. = flux through the barrier

$L = 2.31 \times 10^{-1}$ cm = thickness of barrier

$V = 1\ cm^3$ = unit volume

$\Delta t = 1$ sec. = unit time

$A = 3.17 \times 10^{-1}\ cm^2$ = area of barrier

$C_1 = 9.47 \times 10^{17}$ atoms/cc = concentration of krypton atoms on upstream side of barrier

C_2 = (taken as zero) = concentration of krypton on downstream side of barrier

$$D = \frac{(3.5 \times 10^{7})(2.31 \times 10^{-1})}{(3.17 \times 10^{-1})(9.47 \times 10^{17})} = 2.7 \times 10^{-11}\ cm^2/sec.$$

Activation Energy

The activation energy, E_a, was determined by use of the equation:

$$\ln D = \ln D_o - E_a/k(1/T) \tag{16}$$

by forming two equations in two unknowns:

$$\ln D_1 = \ln D_o - E_a/k(1/T_1) \tag{17}$$

and

$$\ln D_2 = \ln D_o - E_a/k(1/T_2) \tag{18}$$

and subtracting Equation 18 from Equation 17 giving:

$$\ln \frac{D_1}{D_2} = - \frac{E_a\ (T_2 - T_1)}{kT_1T_2} \tag{19}$$

where: $k = 8.616 \times 10^{-5}$ ev/°K = Boltzmann's Constant

evaluated at : $T_1 = 1523$°K, where $D_1 = 5 \times 10^{-11}$ cm^2/sec.

and : $T_2 = 1273$°K, where $D_2 = 2.7 \times 10^{-11}$ cm^2/sec.

$$-E_a = \ln \frac{D_1}{D_2} (kT_1T_2)(T_2 - T_1)$$

$$-E_a = \frac{\ln 1.85(8.616 \times 10^{-5})(1.273 \times 10^3)(1.523 \times 10^3)}{1273 - 1523}$$

$$-E_a = \frac{(6.15 \times 10^{-1})(8.616 \times 10^{-5})(1.273 \times 10^3)(1.523 \times 10^3)}{-250}$$

$$E_a = 0.412 \text{ ev}$$

Diffusion Constant

The diffusion constant, D_o, was calculated using rearranged Equation 11 to give:

$$\ln D_o = \ln D + E_a/kT \tag{20}$$

or: $D_o = D \exp (E_a/kT)$

$D_o = 5 \times 10^{-11} \exp (3.18)$

$D_o = (5 \times 10^{-11})(2.4047 \times 10^{1})$

$D_o = 1.2 \times 10^{-9}$ cm^2/sec.

APPENDIX D

Theoretical Calculation of Activation Energies for Movement of Ne and Kr Atoms Through Vacancies and Edge Dislocations in Alpha Alumina.

The "Method of Moody"[35] was used to calculate a theoretical value for the activation energies for the movement of Ne and Kr through vacancies and edge dislocations in alpha alumina. These values were obtained by considering the inert gas atoms as tunneling through the oxygen structure of alpha alumina with the tunnel being formed by missing oxygen atoms in the case of vacancies and by misalignment of oxygen atoms in the case of edge dislocations. The atoms adjacent to these lattice defects were considered as possessing imaginary springs with compressional and tensil values based on Young's modulus of elasticity for alpha alumina. The activation energy was considered as being that which was required to compress the atoms to such an extent as to enlarge the hole or vacancy in the plane of oxygen atoms and allow the inert gas atom to pass through. The fundamental equation was as follows:

$$\frac{\text{Force}}{\text{Area}} = y \frac{\Delta L}{L}$$

where Area = λ^2, when λ is the oxygen atomic diameter and equal to 2.64×10^{-8} cm

Force = $k\Delta\lambda$, where k is a constant for the imaginary spring and $\Delta\lambda$ is movement in compression or in tension as the inert gas atom passes through

y = Young's modulus of elasticity for alpha alumina = 3.87×10^{9} gms/cm^2

ΔL = change in length

L = total length

This leads to:

$$\frac{k\Delta\lambda}{\lambda^2} = y\,\frac{\Delta L}{L}$$

where $k = y\lambda$

Since: Work = Force X Distance

the theoretical activation energy may be calculated by integrating the expression $k\lambda d\lambda$ over the range of oxygen distortion.

Figure 24 shows probable arrangements for the oxygen atoms around an edge dislocation and a vacancy in a plane of hexagonal close packed arrangement. Krypton and neon atoms were superimposed to scale upon these defects to show the amount of distortion required of the oxygen atoms to allow passage of the neon and krypton atoms. The total distortion of the oxygen atoms in each case was expressed as a fraction of the diameter of oxygen. The measured distortions around both types of defects for neon and krypton are given in Table 10. Table 10 also gives the calculated theoretical activation energies for these processes. A sample of the theoretical calculation of activation energy for neon through an edge dislocation in one plane of oxygen atoms in alpha alumina follows:

$$W = \int_0^{\frac{7}{19}\lambda} k\lambda\, d\lambda = \frac{1}{2} k\lambda^2 \Big|_0^{\frac{7}{19}\lambda} = \frac{1}{2} k \left(\frac{7}{19}\lambda\right)^2$$

$$= \frac{1}{2} y\lambda^3 \left(\frac{7}{19}\right)^2$$

$$W = (.5)(5.5 \times 10^{7} \text{ lbs/in}^2)(2.64 \times 10^{-8} \text{ cm})^3 (3.68 \times 10^{-1})^2$$

$$= 6.84 \times 10^{-17} \text{ lbs cm}^3/\text{in}^2$$

$$= (6.84 \times 10^{-17} \text{ lbs cm}^3/\text{in}^2)(6.8947 \times 10^{4} \text{ dynes in}^2/\text{cm}^2 \text{ lbs})$$

$$= 47.2 \times 10^{-13} \text{ dyne cm} = 4.72 \times 10^{-12} \text{ ergs}$$

$$= (4.72 \times 10^{-12} \text{ ergs})(6.2422 \times 10^{11} \text{ ev/erg})$$

$$= 2.94 \text{ ev}$$

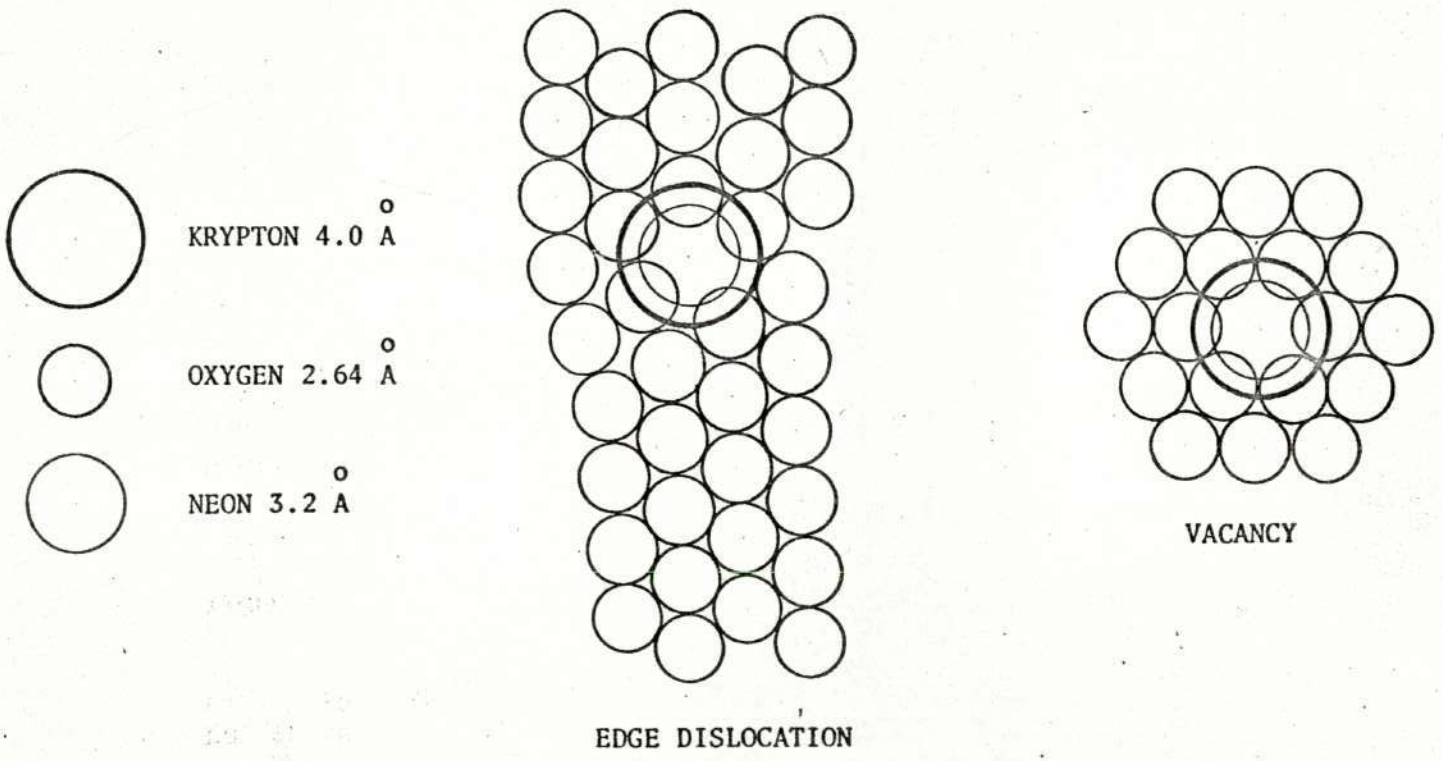

Figure 24. Oxygen Arrangements Around Defect Structures in FCC Plane of Alpha Alumina

Table 10

Measured Distortions in Plane of HCP Oxygen Due to Passage of Ne and Kr Through Vacancy and Edge Dislocations Defects, Also Theoretical Values of Activation Energies for the Above Processes.

	Neon	Krypton
Distortion around a vacancy defect expressed as a fraction of O^{-2} diameter, λ	$(34/19)\lambda$	$(105/19)\lambda$
Distortion around an edge dislocation defect (fraction of O^{-2} diameter, λ	$(7/19)\lambda$	$(79/19)\lambda$
Theoretical activation energy at vacancy (ev)	69.5	663
Theoretical activation energy at edge dislocation (ev)	2.94	376

CHAPTER VIII

BIBLIOGRAPHY

1. Bernard, Michael F., "A Selected Bibliography on Diffusion in Ceramic Systems", from Research and Development Report: "Metals, Ceramics and Materials" (UC-25) TID 4500, December 15, 1960, published by Ames Laboratory of Science and Technology, Iowa State University, IS-448, May, 1962.

2. Jost, W., "Diffusion in Solids, Liquids, Gases", p. 1, Academic Press, Inc., 111 Fifth Avenue, New York, New York, 1960.

3. Kingery, W. D., "Introduction to Ceramics", pp. 198-201, John Wiley and Sons, Inc., 605 Third Avenue, New York, New York, 1960.

4. Sinnott, M. J., "The Solid State for Engineers", pp. 350-351, John Wiley and Sons, 605 Third Avenue, New York, New York, 1959.

5. Shewmon, P. G., "Diffusion in Solids", p. 44, McGraw-Hill Book Company, Inc., 330 W. 42nd Street, New York, New York, 1963.

6. Zener, Clarence, "Ring Diffusion in Metals", Acta Crystallographica, Vol. 3, 346, 1950.

7. Kingery, W. D., op. cit., p. 219.

8. Darken, L. S., "Formal Basis of Diffusion Theory from Atom Movements", pp. 1-8. A seminar held during the Thirty-second National Metal Congress and Exposition, Chicago, October 21 to 27, 1950, Published by the American Society for Metals, Cleveland, Ohio.

9. Barrer, Richard M., "Diffusion in and Through Solids", p. 12, Cambridge University Press, 32 E. 57th Street, New York, New York, 1951.

10. Crank, J., "The Mathematics of Diffusion", pp. 44-46, Oxford University Press, 200 Madison Avenue, New York, New York, 1951.

11. Zener, C., "Theory of D_o for Atomic Diffusion in Metals", pp. 372-375, Journal of Applied Physics, Vol. 22, No. 4, April, 1951.

12. Buckley, H. E., "Crystal Growth", pp. 98-102, John Wiley and Sons, 605 Third Avenue, New York, New York, 1951.

13. Krunberg, M. L., "Plastic Deformation of Sapphire", Acta Metallurgica, Vol. 5, pp. 507-511, 1957.

14. Wycoff, R. W. G., "Crystal Structure", pp. 3-4, Interscience Publishers, 605 Third Avenue, New York, New York, 1951.

15. Gray, T. J., "The Defect Solid State", pp. 93-118, Interscience Publishers, 605 Third Avenue, New York, New York, 1957.

16. Kuczynski, G. C., Albernethy, L., Allan, J., "Sintering Mechanisms of Aluminum Oxide", pp. 163-172 of "Kinetics of High Temperature Processes", edited by W. D. Kingery, Technology Press and John Wiley and Sons, 605 Third Avenue, New York, New York, 1959.

17. Burke, J. E., "Grain Growth in Ceramics", pp. 109-116 of "Kinetics of High Temperature Processes", edited by W. D. Kingery, Technology Press, and John Wiley and Sons, 605 Third Avenue, New York, New York, 1959.

18. Cutler, I. B., "Nucleation and Nuclei Growth in Sintered Alumina", pp. 120-127 of "Kinetics of High Temperature Processes", edited by W. D. Kingery, Technology Press and John Wiley and Sons, 605 Third Avenue, New York, New York, 1959.

19. Coble, R. L., "Diffusion Sintering in the Solid State", pp. 147-163 of "Kinetics of High Temperature Processes", edited by W. D. Kingery, Technology Press and John Wiley and Sons, 605 Third Avenue, New York, New York, 1959.

20. Linde Industrial Crystals Bulletin No. 3, "Properties of Industrial Sapphire", dated December 18, 1956.

21. Linde Air Products Company Memo, dated February 14, 1957, "Semi-Quantitative Spectrochemical Analysis of Sapphire Boules".

22. Newsome, I. W., Heiser, H. W., Russell, A. S., Stumpf, H. C., "Alumina Properties", p. 33, Technical No. 10 (2nd revision), Alcoa Research Laboratories, 1960.

23. Sinnott, M. J., "The Solid State for Engineers, pp. 253-257, John Wiley and Sons, 605 Third Avenue, New York, New York, 1958.

24. Selig, H., Malm, J. G., and Claassen, H. H., "The Chemistry of the Noble Gases", Scientific American, Vol. 210, No. 5, May, 1964.

25. Linde Company, "Linde High-Purity Gases for Nuclear Processes", Linde Company, Division of Union Carbide Corporation, 30 East 42nd Street, New York 17, New York, no date.

26. Meggers, W. F., "Key to Periodic Chart of the Atoms", W. M. Welch Scientific Company, 1954.

27. Oishi, Y. and Kingery, W. D., "Self-Diffusion of Oxygen in Single Crystal and Polycrystalline Aluminum Oxide", Journal of Chemical Physics, Vol. 33, No. 2, August, 1960.

28. Hayes, D., Budworth, D. W., Roberts, J. P., "Selective Permeation of Gases through Dense Sintered Alumina", Transactions of the British Ceramic Society, Vol. 60, No. 7, July, 1961.

29. Barrer, R. M., op. cit., pp. 412-413.

30. Campbell, W. B., "Diffusion Rate and Activation Energy of Helium Through Single Crystal and Polycrystalline Alumina", unpublished M.S. thesis, Georgia Institute of Technology, 1960.

31. Hurst, J. J., "Helium Diffusion, Permeation Rate and Activation Energy for Polycrystalline Alumina", unpublished M.S. thesis, Georgia Institute of Technology, 1961.

32. Harrington, D. B., "Time-of-Flight Mass Spectrometry", from "Encyclopedia of Spectroscopy", edited by Dr. C. F. Clark, Reinhold Publishing Corporation, 430 Park Avenue, New York, New York, 1960.

33. Wiley, W. C., McLaren, I. H., "Time-of-Flight Mass Spectrometer with Improved Resolution", Review of Scientific Instruments, Vol. 26, p. 1150, 1955.

34. Linde Company, Industrial Crystals Bulletin titled "Linde Alumina Abrasives", March 15, 1961.

35. Moody, W. E., Whitehead, W. D. and Kriegel, W. W., "Activation Energy for Diffusion of Xe^{133} Through MgO-Ni Cermet Compacts", Journal of the American Ceramic Society, Vol. 43, pp. 634-640, December, 1960.

36. Rama, S. N. I., Hart, S. R., "Neon Isotope Fractionation During Transient Permeation", Science, Vol. 147, pp. 737-738, February, 1965.